Invited Research Article, JVGR

Challenging dyke ascent models using novel laboratory experiments: Implications for reinterpreting evidence of magma ascent and volcanism

Janine L. Kavanagh[*a], Alec J. Burns[b], Suraya Hilmi Hazim[a], Elliot Wood[a], Simon A. Martin[a], Sam Hignett[a] and David J.C. Dennis[b]

[a] Department of Earth, Ocean and Ecological Sciences, University of Liverpool, Liverpool L69 3GP, United Kingdom

[b] School of Engineering, University of Liverpool, Liverpool L69 3GH, United Kingdom

[*] Corresponding author: Janine.Kavanagh@liverpool.ac.uk

Abstract

Volcanic eruptions are fed by plumbing systems that transport magma from its source to the surface mostly fed by dykes. Here we present laboratory experiments that model dyke ascent to eruption using a tank filled with a crust analogue (gelatine, which is transparent and elastic) that is injected from below by a magma analogue (dyed water). This novel experimental setup allows, for the first time, the simultaneous measurement of fluid flow, sub-surface and surface deformation during dyke ascent. A penny-shaped fluid-filled crack is formed, intrudes and traverses the gelatine slab vertically to then erupt at the surface. Polarised light shows the internal stress evolution as the dyke ascends, and an overhead laser scanner measures the surface elevation change leading to dyke eruption. Fluorescent passive-tracer particles illuminated by a laser sheet are monitored, and the intruding fluid's flow dynamics and gelatine's sub-surface strain evolution is measured using particle image velocimetry and digital image correlation, respectively. We identify 4 previously undescribed stages of dyke

ascent. Stage 1, early growth: the initial dyke grows from the source, and two fluid jets circulate as the penny-shaped crack is formed. Stage 2, pseudo-steady growth: characterised by the development of a rapidly uprising, central, single pseudo-steady fluid jet as the dyke grows equally in length and width and the fluid down-wells at the dyke margin. Sub-surface host strain is localised at the head region and the tail of the dyke is largely static. Stage 3, pre-eruption unsteady growth: an instability in the fluid flow appears as the central fluid jet meanders, the dyke tip accelerates towards the surface and the tail thins. Surface deformation is only detected in the lead up to eruption and is characterised by an overall topographic increase, with axis-symmetric topographic highs developed above the dyke tip. Stage 4 is the onset of eruption, when fluid flow is projected outwards and focused towards the erupting fissure as the dyke closes. A simultaneous and abrupt decrease in sub-surface strain occurs as the fluid pressure is released. Our results provide a comprehensive physical framework upon which to interpret evidence of dyke ascent in nature, and suggests dyke ascent models need to be re-evaluated to account for coupled intrusive and extrusive processes and improve the recognition of monitoring signals that lead to volcanic eruptions in nature.

Keywords: Magma flow; host-rock deformation; dyke; analogue experiment; particle image velocimetry; digital image correlation

Highlights

- Laboratory experiments model coupled fluid flow and host deformation during dyke ascent and eruption
- Four stages of dyke propagation are identified: 1) early growth, 2) pseudo-steady, 3) pre-eruption unsteady and 4) eruption
- Pseudo-steady dyke ascent is characterised by a single, central, rapid upward jet with down-flow at the dyke margin; sub-surface strain is concentrated at the dyke head and the tail is static
- Unsteady flow occurs as the dyke tip approaches the surface and the tail contracts; surface deformation leading to eruption produces axis-symmetric topographic highs above the ascending dyke tip
- Pressure release during eruption forces all fluid upwards and out of the fissure and the dyke contracts

1.0 Introduction

Nearly all volcanic eruptions are fed by magma-filled fractures that propagate through the crust. The dynamics and propagation of magma intrusions has direct influence on the style, longevity and climatic impact of volcanic eruptions by modulating the supply, ascent rate and rheology of magma that reaches the surface (e.g. Caricchi et al. 2014a,b; Ilyinskaya et al. 2017). Magma intrusion precedes volcanic activity (e.g. Patane et al. 2002), can trigger an eruption (e.g. Sigmundsson et al. 2010), occurs during volcanism (e.g. Castro et al. 2016) and is active in repose periods between eruptions (e.g. Wright et al. 2012). The majority of dykes do not erupt (e.g. Crisp 1984; Gudmundsson, 2002) and diverse geophysical, geochemical and geodetic techniques can be readily employed to monitor magma intrusion in the build up to and during volcanic crises, e.g. retrieving seismic profiles, recording volcanic gas emissions, and detecting surface changes in elevation as the magma-filled fractures grow (e.g. Sparks et al. 2012). However, our ability to interpret this data depends on, and is limited by, the validity of model assumptions and field observations.

Volcanic plumbing systems comprise a network of interconnected magma intrusions that vary in orientation relative to stratigraphic layering and span orders of magnitude in volume and aspect ratio (see the collection of papers in the Special Volume by Menand et al. 2011 for a review). Dykes are vertical to sub-vertical magma-filled fractures that have high aspect ratio (length/thickness), cut across bedding planes of rock strata, and are the primary conduit to transport magma through the crust to potentially erupt (e.g. Geshi et al. 2010; Gudmundsson 2006). The rock record provides access to ancient volcanic plumbing systems through field studies of the solidified remnants of magma and deformed surrounding host rock in 2D (e.g. Gudmundsson 2003) and rarely in 3D (e.g. Kavanagh and Sparks 2011). However, only a

78 partial record will be preserved and it can be difficult to distinguish pre-, syn- and post-
79 magma intrusion processes. Studying dyke propagation in nature is challenging as only
80 remote measurements can be made during an intrusive event. Evidence of recent dyking has
81 been garnered through geophysical and geodetic measurements of intrusions related to on-
82 land rifting, e.g. Afar and Iceland (Wright et al. 2012). The 2014 dyke intrusion associated
83 with the Bardarbunga volcanic system (e.g. Sigmundsson et al. 2014; Gudmundsson et al.
84 2014) is arguably the most detailed study of an individual dyking event that led to a fissure
85 eruption. Along with studies of eruptive episodes on Etna, Italy (e.g. Gonzalez et al. 2014, Kahl
86 et al. 2011) and Kilauea, Hawaii (e.g. Cervelli et al. 2002) for example, it has done much to
87 shape and inform our understanding of the geophysical signals of magma intrusion that leads
88 to eruption.

89 Magma ascends through the crust in regional dykes from deep magma reservoirs primarily
90 due to buoyancy; dyke ascent in nature represents the release of gravitational potential
91 energy on a planetary scale (see Putirka (2017) for a review) and the release of elastic energy
92 on a regional scale. Magma ascent in dykes is facilitated or impeded by the ability of the
93 magma to flow (its rheology) and deformation of mechanically layered and fractured crustal
94 rocks to accommodate the intrusion. Analogue experimentation and numerical modelling are
95 complementary methods to aid the interpretation of field studies and geophysical surveys of
96 magma intrusion (see Rivalta et al. (2015) and Kavanagh et al. (In Review) for reviews). These
97 dyke propagation models have considered a range of physical processes that impact dyke
98 ascent, including magma buoyancy (e.g. Takada 1990; Rivalta et al. 2005; Taisne and Jaupart
99 2009), solidification (e.g. Taisne and Tait 2011), deformation of the host material (e.g.
100 Abdelmalak et al. 2012, Kavanagh et al. 2015), interaction with a load or stress field
101 (Watanabe et al. 2002; Daniels & Menand 2015; Menand et al. 2010; Maccaferri et al. 2014;

Pinel & Jaupart 2000), mechanical layering (e.g. Kavanagh et al. 2006) and pre-existing structures or weak boundaries (e.g. Le Corvec et al. 2013a; Kavanagh et al. 2017). Technical challenges have meant that analogue experiments have studied either the magma or the host solid, and yet the coupled nature of dyke intrusion means that the simultaneous quantification of both aspects is needed.

In this invited paper, here we describe a new series of novel laboratory experiments where, for the first time, coupled magma flow and host rock deformation is studied during dyke initiation, propagation and eruption. By quantifying flow velocity within the analogue magma with contemporaneous surface deformation and sub-surface strain and stress evolution, we identify previously unrecognised processes that relate the interaction of the intruding magma with its host material to dyke propagation dynamics. We discuss our results in the context of the potential of the rock record to preserve both flow dynamics in crystalline fabrics and evidence of sub-surface deformation during magma intrusion, challenging existing dyke models that are used to interpret surface deformation related to magma intrusion that leads to eruption.

2.0 Experimental setup and data processing methods

2.1 Gelatine preparation, Young's modulus measurement and scaling

To prepare an experiment, forty litres of 2.5 wt% concentration gelatine was made following the guidelines of Kavanagh et al. (2013). To dissolve the mixture, one kilogram of gelatine powder (260 Bloom, 10 mesh, pig-skin gelatine supplied by Gelita UK) was mixed with 19 kg distilled water at approximately 90 ºC, and this was then diluted further by 20 kg of cold distilled water to create the final desired concentration. Distilled water was used to inhibit bacterial growth and to ensure no impact of local water composition on the gelatine's

125 properties, which has been shown to be susceptible to pH (e.g. Djabourov et al. 1988, Brizzi
126 et al. 2016). In its sol-state (liquid), the hot gelatine mixture was poured into a clear-Perspex
127 square-based tank measuring 40 x 40 x 30 cm^3 (see Figure 1), any bubbles were then removed
128 from the surface, and the surface was covered in a thin layer of oil to stop dehydration and
129 the development of a tough 'skin'. The experiment tank was then covered in a layer of plastic-
130 wrap and placed into a refrigerator at 5 ºC to cool and solidify for approximately 20 hours
131 (see Table 1).

132 The Young's modulus of the gelatine solid was measured immediately prior to running an
133 experiment. To do this the experiment tank was taken out of the refrigerator and the plastic
134 wrap and oil layer was removed. A brass cylindrical load (see Table 2) was then placed in
135 centre of the gelatine's surface, and the deflection it caused was measured using a digital
136 micrometer. Following the guidelines from Kavanagh et al. (2013), the diameter of the load
137 was small compared to that of the experiment tank, and the mass was sufficient to cause a
138 measureable deflection (±0.005 mm). The Young's modulus *E* was then calculated using the
139 following equation (Kavanagh et al. 2013):

140 $$E = \frac{mg(1-\nu^2)}{D\omega} \quad [1]$$

141 where *m* is the mass of the experiment load, *g* is gravity, ν is Poisson's ratio of the gelatine
142 (0.5, according to Righetti et al. 2004), *D* is the load diameter and ω is the deflection it causes
143 to the gelatine's surface. For each experiment, an average of measurements is reported
144 (Table 1) based on two different loads (Table 2) and three measurements per load.

145 Kavanagh et al. (2013) showed that gelatine mixtures in the gel-state (2-5 wt% and 5-10 ºC)
146 that are injected by water can be appropriately scaled to model dyke propagation in nature.

147 They defined a series of scale factors based on the assumption that the characteristic length
148 scale of the experiment is the buoyancy length L_b, which is the length of the fracture when
149 the buoyancy forces balance the resistive forces of the fracture (Taisne and Tait 2009):

150 $$L_b = \left(\frac{K_c}{\Delta\rho}\right)^{\frac{2}{3}}, \quad [2]$$

151 where K_c is the fracture toughness and $\Delta\rho$ is the density difference between the intruded fluid
152 and the host material. From this follows four scale factors (Kavanagh et al. 2013):

153 Length scale L*:

154 $$L^* = \frac{L_l}{L_n} = \left(\frac{K_c^*}{\Delta\rho^*}\right)^{\frac{2}{3}}, \quad [3]$$

155 Timescale T*:

156 $$T^* = \frac{T_l}{T_n} = \rho_{solid}^{*\frac{1}{2}} K_c^{*\frac{1}{3}} (\Delta\rho)^{-\frac{5}{6}}, \quad [4]$$

157 Velocity scale U*:

158 $$U^* = \frac{U_l}{U_n} = (\Delta\rho^*)^{\frac{1}{6}} K_c^{*\frac{1}{3}} \rho_{solid}^{*-\frac{1}{2}}, \quad [5]$$

159 and Stress scale E*:

160 $$E^* = \frac{E_l}{E_n} = \Delta\rho^* L_b^* \left(\frac{L_b}{\psi}\right)^*, \quad [6]$$

161 where subscript *l* is in the laboratory, subscript *n* is in nature, ρ_{solid} is the density of the host
162 material and ψ is the thickness of the intrusion. In our experiments where water is injected
163 into gelatine: L* = 2 x 10^{-3}, and so 1 m in experimental dyke length corresponds with 500 m
164 of dyke length in nature; T* = 9 x 10^{-2}, meaning 1 second of the experiment corresponds to
165 11 seconds in nature; and U* = 2 x 10^{-2}, such that 0.001 m/s in the experiment represents
166 0.05 m/s in nature. Kavanagh et al. (2013) found that E* = 2 x 10^{-6} to 2 x 10^{-5}, and as our
167 laboratory measurements of Young's modulus span 2000-3000 Pa (Table 1) this corresponds
168 to rocks in nature that have a Young's modulus of 0.1-1.5 GPa. These values are geologically

169 reasonable and so support the preface that scaled gelatine experiments can be used to
170 describe magma intrusion in nature.

171 *2.2 Experimental Setup*

172 An experiment is run by injecting water through the base of the solid gelatine slab, using a
173 tapered syringe connected to a peristaltic pump that delivers fluid at a constant volumetric
174 flux (see Table 1). A valve connected to the injection system and a small petroleum jelly seal
175 at the injector tip ensures only water and no air is injected. The orientation of the dyke that
176 is formed is controlled by making a small, vertical cut in the base of the gelatine and inserting
177 the injector into this. It is ensured that the tapered edge of the injector is orientated parallel
178 to the crack. To this basic setup, additional imaging apparatus are used and these are
179 described in more detail in the following sub-sections. These include: gelatine stress field
180 analysis, surface elevation change, dynamics of the intruding fluid flow using particle image
181 velocimetry (PIV), and sub-surface strain analysis via digital image correlation (DIC).

182 *2.2.1 Photoelasticity and surface deformation*

183 Polarising sheets are attached to the outside of the experiment tank, on opposite sides and
184 perpendicular to the dyke strike direction (x-z plane, see Figure 1a). Gelatine solids are
185 photoelastic, meaning that qualitative stresses and their evolution can be visualised using
186 polarised light. Two light sources illuminate the tank from behind, and two HD video cameras
187 are used to record the sub-surface growth of the experimental intrusions; one is positioned
188 to record the polarised-light view (HD-1, x-z plane), and one images the plane of the dyke in
189 artificial light (HD-2, y-z plane). An additional HD video camera positioned above the
190 experiment tank monitors the free-surface of the gelatine (HD-3, x-y plane). Footage from
191 cameras HD-1 and HD-2 were analysed using the open source software Tracker (Version 4.96)

192 to measure the dyke length, width, and tip position relative to the surface of the gelatine over
193 time.

194 To monitor the changes in surface topography over time, a Micro-Epsilon laser scanner (L1)
195 is positioned above the analogue setup (Figure 1a). The laser projects a thin, vertical sheet of
196 light onto the surface of the gelatine; this produces a red line on the gelatine surface that is
197 positioned perpendicular to the dyke strike direction and centred on the injector port. As the
198 gelatine solid is transparent, a thin layer of dark-coloured fine sand (approximate particle size
199 0.25 mm) is spread evenly over the surface of the gelatine to aid deflection of the laser light.
200 The software ScanCONTROL 5.0 is used to collect data along a 140 mm long transect, with
201 measurement points positioned every 0.5 mm along the projection. Each point along the
202 projection is assigned a height value that corresponds to the distance between the surface of
203 the gelatine and the source of the laser sheet. Changes in the surface topography are
204 recorded at timed intervals of 4 scans per second.

205 After the experiment, data from the Micro Epsilon laser scanner is exported and manipulated
206 in MATLAB (by Mathworks). Sub-sampling of the dataset produces an elevation profile in 10
207 second intervals. The cumulative sum of displacement is then calculated across the horizontal
208 transect to illustrate the change in topography over time. Using the statistical analysis
209 software R, a non-parametric fit LOESS curve (Locally Weighted Scatterplot Smoothing) is
210 applied with a span width of 0.3 for the smoothing window.

211 *2.2.2 Particle image velocimetry (PIV) and digital image correlation (DIC)*

212 PIV or DIC are used to quantify fluid flow velocities within the injected fluid or sub-surface
213 strain evolution in the intruded gelatine, respectively. A New Wave Solo-PIV III Laser (L2)

214 provides 50 mJ of energy per pulse at 15 Hz, with a pulse width of 3-5 ns and a wavelength of
215 532 nm. The laser fires at a repetition rate of 8.875 Hz for the PIV fluid flow experiments
216 (Figure 1b) and 1 Hz for the DIC gelatine sub-surface deformation experiments (Figure 1c).
217 The laser light is formed into a thin sheet (approximately 1 mm thick) using a cylindrical lens
218 which excites 20-50 μm fluorescent, spherical poly(methyl methacrylate) (PMMA) particles
219 with a Rhodamine-B coating that gives peak fluorescence at a wavelength of 590 nm. The
220 laser sheet is fired from the side of the tank and positioned vertically so it intersects with the
221 injection point (Figure 1b, c).

222 The passive tracer particles are mixed into the injection fluid (Figure 1b) or the host gelatine
223 during preparation of the experiment (Figure 1c). Particles within the injecting fluid are added
224 immediately prior to injection, and the fluid is kept in a container placed on a magnetic stirrer
225 to ensure they remain in suspension during extraction. The particles are slightly denser than
226 water and so over time they settle out of suspension, although this occurs over 10's of
227 minutes and so is beyond the time of an individual experiment. The fluorescent particles are
228 added to the hot gelatine mixture prior to it being left to cool, stirring it continuously before
229 being placed in the refrigerator when it reaches 21 ºC. This ensures an even distribution of
230 the tracer particles within the solidified gelatine.

231 Images are captured using a 2 MP CCD camera fitted with a 35 mm Nikon lens (Figure 1b, c).
232 The light reflected from the experiment is filtered using an optical longpass filter, which
233 passes light with a long wavelength and blocks short wavelengths with a cut-in wavelength of
234 550 nm. This prevented the laser light that was reflected by the gelatine from entering the
235 camera, thus allowing the light from the fluorescent particles to be clearly observed.

236 *2.2.2.1 Calibration and pre-processing*

Before each PIV or DIC experiment, an image is acquired of a 2D calibration target (an array of evenly-spaced black dots on a white background) aligned with the laser sheet and situated in the tank filled with water. Dantec Dynamic Studio imaging software detects the position and size of the filled-circles, and defines the area across which quantitative analysis can be accurately performed. This calibration image is later used in pre-processing to dewarp images of the experiment that are acquired. This process corrects for any distortion (which is minimal in our experiments and only occurs around the edges of the camera image; areas which are of little interest) as well as providing an accurate conversion between pixels and physical space. Great care is taken to ensure that the camera location, camera focus, tank location and laser sheet are not altered between this calibration step and the experiment itself.

2.2.2.2 Data processing and post-processing

After dewarping (described above) PIV cross-correlations produce vector fields (e.g. Adrian, 1991) using Dantec Dynamic Studio software. We utilise an adaptive correlation technique in which the interrogation windows have a 50% overlap. This results in a distance between vectors of 1.8 mm. Spurious vectors are removed using standard range and moving average validation techniques, and replaced with local mean values.

Post-processing of the vector fields is conducted in Matlab. As the region of interest increases in size throughout the experiment as the intrusion grows, we developed a masking technique that creates and applies a different mask for every PIV vector field. This is based on the region of interest being identified in the experimental images using an intensity threshold. This processing step eliminates vectors outside the region of interest that are purely the result of measurement noise.

For visualisation purposes only (figures and movies) a 3-by-3 spatial box is applied to the vector fields before plotting. In addition, it is evident that long time-averaging is not possible due to the constantly varying size of the intrusion. However, given that the timescale of the growth of the intrusion is significantly longer than the PIV capture rate we can average over a limited number of frames (10) such that each plot (or movie frame) is a short time-average (i.e. spanning 1.13 s in the PIV dyke flow experiments). Finally, to improve the clarity of the vectors in the visualisations, they are down-sampled by a factor of two (i.e. only every second vector is plotted) or three, depending on the type of experiment and visualisation. The colour-maps in all cases are not down-sampled and reflect the resolution of the experiments.

In the DIC experiments, strain is calculated from the post-processed vector field data. For the small strains in the sub-surface gelatine (significantly less than unity) the strain tensor can be linearised to give Cauchy's infinitesimal strain tensor:

$$\epsilon_{ij} = \frac{1}{2}\left(\frac{\partial \mathbf{v}_i}{\partial \mathbf{x}_j} + \frac{\partial \mathbf{v}_j}{\partial \mathbf{x}_i}\right) \quad [7]$$

where **v** is the displacement vector, and **x** is the spatial coordinate. Thus, in the two-dimensions of interest in the DIC experiments, *u* and *w* are vector displacements in the x- and z- directions, respectively,

$$\epsilon_{xx} = \frac{\partial u}{\partial x}, \quad [8]$$

and

$$\epsilon_{zz} = \frac{\partial w}{\partial z} \quad [9]$$

for the normal components of strain ϵ.

279 The shear components are equal due to symmetry, so,

$$\epsilon_{xz} = \epsilon_{zx} = \frac{1}{2}\left(\frac{\partial u}{\partial z} + \frac{\partial w}{\partial x}\right). \quad [10]$$

280

281 As the DIC provides discrete data on an even grid we simply estimate the gradients using a

282 central differencing scheme, such that,

$$\epsilon_{xx} \approx \frac{u_{n+1,m} - u_{n-1,m}}{2\Delta x}, \quad [11]$$

283

$$\epsilon_{zz} \approx \frac{w_{n,m+1} - w_{n,m-1}}{2\Delta z} \quad [12]$$

284

285 and,

$$\epsilon_{xz} \approx \frac{1}{2}\left(\frac{u_{n,m+1} - u_{n,m-1}}{2\Delta z} + \frac{w_{n+1,m} - w_{n-1,m}}{2\Delta x}\right) \quad [13]$$

286

287 where ϵ_{xx} is the strain at the location (*n, m*). Note that $\Delta x = \Delta z$ as the PIV interrogation

288 windows are square; where Δx and Δz are the spacing between the vectors in the x and z

289 directions, respectively. The error introduced by the discretisation of the equations is second

290 order, $O(\Delta x^2)$.

291 **3.0 Results**

292 The same experiment was carried out four times; each had the same gelatine concentration,

293 volume and injection method but a different imaging techniques was applied (see Table 1).

294 Across the different techniques, we have identified four stages of dyke growth to eruption:

295 1) dyke inception, 2) dyke propagation, 3) pre-eruption ascent and 4) fissure eruption. The

296 appearance of these different stages is now described in detail for each technique.

297 *3.1 Dyke propagation geometry and sub-surface stress*

298 A penny-shaped water-filled fracture was produced during injection. This experimental dyke
299 propagated vertically (+/- 10º) towards the surface. Although qualitative, polarised light is
300 very useful to demonstrate the evolving stress field during dyke propagation using the
301 photoelastic properties of gelatine. Coloured fringes depict stress contours, with high
302 concentration of these indicating increasing stress intensity. The developing stress field and
303 its distribution around the growing dyke is shown in Figure 2 and Supplementary Video Figure
304 1, showing stress is concentrated at the dyke tip and producing a 'bow-tie' of stress contours
305 in the x-z plane (Figure 2i and ii). The visually-stressed region of gelatine is initially localised
306 (Figure 2ai, ii), but increases in extent as the dyke ascends (Figure 2bi, ii). Towards the surface,
307 the stress field begins to intersect the surface and this continues to eruption (Figure 2ci, ii).

308 Three stages of pre-eruption dyke growth can be identified based on the growing dyke
309 geometry. Dyke length and width measurements based on HD video images (e.g. Figure 2 iii)
310 and are shown in Figure 3a. In Stage 1 a circular geometry is developed (Figure 2aiii), and this
311 corresponds with approximately equal dyke length and width (Figure 3a) although the rate of
312 their growth decelerates over approximately the first 100 seconds of the experiment (Figure
313 3b). In Stage 2, the dyke length and width continue to steadily grow at approximately
314 constant velocity (Figure 3b). Stage 3 marks the lead up to eruption, where the dyke begins
315 to accelerate towards the surface, its length increases at a faster rate than its width, and it
316 develops an elliptical geometry towards eruption (Figure 2iii, c). At stage 4 the dyke tip
317 reached the surface and it erupted to form a short fissure, and fluid was extruded onto the
318 gelatine surface. The fissure measured approximately 5 cm in length, and the fissure margins
319 were practically closed with an opening <0.1 mm through which fluid flowed. The data
320 presented in Figure 3 are from two identical experiments (Table 1), and they demonstrate the
321 high degree of reproducibility between experiments.

3.2 Mapping fluid flow with a propagating and erupting dyke

In PIV experiments, passive tracer particles suspended in the injected fluid fluoresced in the y-z plane of the experimental dyke (see Supplementary Video Figure 2a). Based on the fluid dynamics, the dyke propagation can be described in four stages (see Figure 4 and Supplementary Video Figure 2b):

Stage 1: Fluid flow vectors within the first minute of experimental dyke growth were complex, but organised into two jets; one making a curved trajectory that is clockwise near the base of the injector, and the other moving in an anti-clockwise direction in the upper part of the dyke at the dyke margin (Figure 4a). At this time the dyke was small (approximately 70 mm wide and 70 mm high), far from the gelatine surface (160 mm depth) and close to the injector, with a maximum flow velocity of 14.6×10^{-3} m/s.

Stage 2: After the initial dyke growth, the dyke fluid flow stabilises into one pseudo-steady, upward rising jet along the centre of the dyke (Figure 4b). Flow velocities are maximum close to the injector, but the maximum flow speed has reduced to 6.6×10^{-3} m/s compared to stage 1. Flow vectors at the growing tip fan out and rotate to flow downwards at the dyke margin. The slowest flow velocities occur in two elliptical regions between the upward-flowing channel and the down-flowing margin, where the fluid is almost static.

Stage 3: As the dyke approaches the surfaces to erupt, an instability develops in the flow. The central, upward jet meanders from side to side and at the base the fluid flow comprises two upward jets (Figure 4c). The fastest moving fluid has migrated away from the injector and occupies a central band within the growing dyke, with slower velocities at the vertical tip and continued down-flow at the dyke margins. The maximum flow velocities in Stage 3 have

slightly increased compared to stage 2 and are up to 6.9 x 10^{-3} m/s. The two elliptical almost-static fluid regions between the upward jet and dyke margin remain and have grown in size.

Stage 4: The final stage of dyke ascent is the fissure eruption (Figure 4d) when the flow dynamics within the dyke dramatically change. At the onset of eruption, all flow vectors are rapidly re-oriented upwards and towards the small fissure that formed in the gelatine surface. The upward jet from the injector and two jets at its base remain, though the region of static fluid rapidly increase in size from depth upwards. The fastest flow velocities of all dyke ascent stages are recorded, reaching 32.2 x 10^{-3} m/s as fluid is rapidly expelled and the dyke is drained.

3.3 Sub-surface incremental strain evolution

In DIC experiments, passive-tracer particles within the gelatine solid were illuminated in the x-z plane presenting a cross-section around the growing experimental dyke (see Supplementary Video Figure 3). The laser-illuminated plane reveals sharp margins of the dyke as it grows, and offers the opportunity to record in detail the evolving cross-sectional thickness variation as the dyke grows in addition to quantifying the evolving incremental strain (ϵ_{xx}, ϵ_{zz} and ϵ_{xz}) using DIC. Based on the dyke thickness change and evolution in incremental strain, we identify four stages of dyke growth (Figure 5):

Stage 1: Sub-surface deformation of the gelatine during the early stages of dyke growth show the incremental strain is concentrated at the growing tip (Figure 5a, 55 s). No incremental strain is recorded at the dyke tail region, indicating its opening is maintained. Vector arrows show the gelatine is displaced predominantly at the dyke margins, radiating from the growing tip, with larger lateral than vertical displacement. The largest component of incremental strain occurs in the horizontal direction (ϵ_{xx}); both vertical (ϵ_{zz}) and shear (ϵ_{xz}) components of

367 strain are small. Overall incremental strain intensity in the early stages of dyke growth spans
368 -2 to 12 x 10^{-3} ϵ_{xx}, -2 to 3 x 10^{-3} $\epsilon_{zz,}$ and -2 to 3 x 10^{-3} ϵ_{xz}. Local positive ϵ_{xx} occurs at the dyke
369 tip and local negative ϵ_{xx} occurs adjacent to the dyke tip, whereas local positive ϵ_{zz} occurs just
370 below the dyke tip and local negative ϵ_{zz} just above this. Shear strain is measured around the
371 dyke tip.

372 Stage 2: As the dyke ascends, incremental strain continues to be concentrated at the growing
373 tip and displacement arrows show continued outward radial movement at the dyke head with
374 greater lateral than vertical displacement (Figure 5b, 205 s). Similar patterns of ϵ_{xx}, ϵ_{zz} and ϵ_{xz}
375 occur compared to Stage 1, however their values have all slightly decreased. Uplift of the
376 gelatine free surface is detected by a region of negative ϵ_{zz} developing at the surface.
377 Deflection of the dyke tip from vertical occurs as the dyke begins to propagate in an inclined
378 plane, and this is when an asymmetrical pattern of incremental shear strain (ϵ_{xz}) is detected
379 (lower negative ϵ_{xz} occurs in the upper-right of the dyke tip relative to the lower-left). A small
380 area of negative incremental strain ϵ_{xx} occurs at the dyke tail region. The raw experimental
381 image shows the tail of the dyke has pinched closed. In this stage of dyke propagation, ϵ_{xx}
382 ranges from -1 to 7 x 10^{-3}, ϵ_{zz} ranges from -1 to 2 x 10^{-3}, and ϵ_{xz} ranges from -1.5 to 1.5 x 10^{-3}.

383 Stage 3: Shortly prior to the dyke erupting, the dyke tip remians the focus of incremental
384 strain; but, the magnitude and extent of the strain components significantly changes. The
385 largest strain values are now in ϵ_{zz} rather than ϵ_{xx}. The intensity of negative vertical
386 incremental strain (ϵ_{zz}) has increased in magnitude and extent. Asymmetry in negative ϵ_{xx} is
387 detected at the dyke tip and asymmetry in ϵ_{xz} remains. Small amount of incremental shear
388 strain are detected at the gelatine's free surface. Overall in stage 3, ϵ_{xx} ranges from -1 to 5 x
389 10^{-3}, ϵ_{zz} ranges from -6 to 12 x 10^{-3}, and ϵ_{xz} ranges from -1 to 1.5 x 10^{-3}.

Stage 4: The moment immediately prior to dyke eruption is recorded as opening at the surface and the largest values of ϵ_{xx} are then produced during the experiment. Displacement vectors are oriented towards the surface the surface. Progressive 'zipping' closed of the tail occurs as displacement vectors rotate inwards at depth where small, localised regions of negative ϵ_{xx} are produced. The largest incremental strain occurs in the horizontal component (ϵ_{xx}), followed by the shear strain ϵ_{xz} (which is at its largest at stage 4) and then ϵ_{zz} as the dyke completes its path to the surface. During this stage of dyke ascent ϵ_{xx} ranges from -4 to 14 x 10^{-3}, ϵ_{zz} ranges from -5 to 3 x 10^{-3}, and ϵ_{xz} ranges from -5 to 5 x 10^{-3}.

3.4 Surface deformation during dyke ascent

Figure 6 shows the progressive deformation of the gelatine surface during an experiment as the dyke approached the surface. There was no change in surface topography detected during the majority of dyke ascent (see Supplementary Video Figure 1c), and it was only when the dyke tip reached approximately <4 cm depth (during the final 120 seconds of ascent, see Figure 6a) that an elevation change of the free-surface occurred. By the onset of fissure eruption, there was a gradual overall increase in elevation of 0.5 mm across the whole plane that was monitored. Local topographic highs (up to 1.5 mm) developed either side of the dyke tip (Figure 6b). The elevation change was relatively broad early on, but became increased and focused as the dyke tip approached the surface. The dyke became slightly deflected from its vertical path (as is common in the experiments, e.g. Experiment 2, Figure 5), as shown by an increase in the tip position relative to the injector (Figure 6b). This slightly inclined propagation path resulted in the cumulative surface elevation change not being symmetrical, as the 'hanging wall' of the dyke developed a larger topography (up to 1.5 mm cumulative displacement) than the 'footwall' (approximately 0.9 mm of cumulative displacement).

4.0 Discussion: Coupled processes during dyke ascent and eruption

Most dykes in nature do not erupt (Gudmundsson 2002) and the majority of magmas stall within the crust (Crisp, 1984). Determining if magma will breach the surface is of primary concern for volcanic hazard assessments. Dyke ascent in nature can be studied during ascent or post-emplacement; however, in both cases visualising the three-dimensional evolving geometry of the dyke is challenging and requires extrapolation from often two-dimensional datasets (Kavanagh 2018). Evidence of magma flow, crust deformation and dyke eruption is only partially recorded. Our laboratory experiments can help inform the interpretation of natural data and challenge existing numerical models of dyke ascent.

4.1. Synthesising laboratory experimental results

The range of laboratory experiment monitoring techniques we have employed arguably represent the most detailed and comprehensive description and analysis of coupled fluid flow and host deformation during experimental dyke ascent to eruption. Dyke propagation involves the intrusion of a fluid into a solid, and our results emphasise the strong coupling between the intruding fluid and the deformation of its host-material which influences magma ascent dynamics.

Four common stages of dyke ascent leading to eruption are evident in the experiments. 1) During dyke inception and its early growth, the fluid flow patterns are complex and comprise two circulating fluid jets. Strain is focused at the upper dyke tip as the penny-shape crack is progressively established. 2) As the dyke grows, the fluid flow within it stabilises into a single, rapid and upward flowing jet as the dyke grows in length and width at a constant and steady rate. 3) As the dyke approaches the surface our experiments show a fluid instability develops, causing the upward jet to meander and two jets to form at the dyke base. The origin of this

436 instability is not clear, although its appearance seems to correspond with the time when the
437 dyke tail pinches almost-closed, and when the dyke tip accelerates towards the surface. It is
438 also at this stage that surface deformation is first recorded, resulting in the progressive
439 increase in topography and elevation highs developing above the ascending dyke tip. 4)
440 During dyke eruption, a small fissure is formed at the gelatine surface and a dramatic pressure
441 release induces the rapid evacuation of fluid from the dyke and the dyke walls to 'zip' closed
442 from the tail to the surface.

443 *4.2. Challenging dyke ascent models*

444 The patterns of surface elevation change we measured during dyke ascent agree well with
445 that expected by analytical elastic models; the deformation comprised elevated regions
446 either side of the dyke tip, with a relative low directly above it. Measurements of surface
447 deformation at volcanic centres are often inverted for the source depth and source geometry
448 for example, using simple analytical models that assume intrusion into an isotropic, elastic
449 host-rock. Our experimental observations therefore have the potential to be used to bench-
450 mark these inverse models and inform their development.

451 The numerical models of dyke ascent that have been published can be divided into two end-
452 member approaches (see Rivalta et al., 2015 for a review). Firstly, there are buoyancy-driven
453 dyke ascent models that emphasise elasticity of the intruded media and its fracture
454 toughness. In these models, the dyke becomes disconnected from its source (e.g. Weertman,
455 1971). Secondly, there are flux-driven dyke ascent models where the dyke is connected to its
456 source and the fluid dynamics of the intrusion are described by applying lubrication theory
457 (e.g. Lister, 1990 a, b; and Spence et al. 1987). The circulation of fluid we observe in the
458 experiments agrees well with the flow pattern expected by Dahm's (2000) model, which

459 emphasises the role of elasticity and fracture toughness and reconciles the fluid dynamics of
460 the intruding magma in dyke propagation. However, this flow pattern contrasts with Roper
461 and Lister (2007) who couple fluid flow and host deformation using lubrication theory and a
462 dyke-scale process zone. Their model anticipates that, when connected to the source, dyke
463 fluid flow should be predominantly vertical inside the dyke. However, our results suggest
464 that, despite not having attained their 'buoyant length' and only having a small density
465 contrast between intruding fluid and intruded host, our experimental dykes have the ascent
466 dynamics expected of buoyant fluid-filled fractures in an elastic material, where the
467 mechanical properties of the intruded host dominate the growth dynamics and the viscous
468 resistance of the fluid to flow is minimal.

469 In our experiments, fluid is driven into the dyke at a constant volumetric flux and the dyke
470 remains connected to its source. According to Linear Elastic Fracture Mechanics, the fluid-
471 filled crack will propagate when the fluid overpressure exceeds the fracture pressure P_f of the
472 gelatine solid (Lister and Kerr, 1991):

473 $$P_f = \frac{K_c}{\sqrt{\pi l}}, \qquad [14]$$

474 where K_c is the fracture toughness of the gelatine and l is the crack length. Gelatine's K_c can
475 be estimated by the relationship (Kavanagh et al., 2013):

476 $$K_c = 1.4\sqrt{E}. \qquad [15]$$

477 In our experiments, E = 2000-3000 Pa and so we estimate K_c = 63-77 Pa $m^{1/2}$. However, the
478 density difference between the injected fluid and the intruded gelatine also results in a
479 buoyancy pressure P_b (Rubin, 1995):

480 $$P_b = \left(\rho_s - \rho_{liq}\right) g L_b \, , \qquad [16]$$

481 where ρ_s is the density of the solid (gelatine), ρ_{liq} is the density of the liquid (water), g is gravity
482 and L_b is the buoyant length of the dyke (equation 2) (Taisne and Tait, 2009). Following these
483 relationships, the calculated buoyant length of our experimental dykes is 1.3-1.4 m, where ρ_s
484 = 1002.5 kg/m^3, ρ_{liq} = 998 kg/m^3 and g = 9.81 m/s, which is much greater than the height of
485 the experimental tank (0.3 m). It is therefore expected that the growth of our experimental
486 dykes is flux-driven, and any buoyancy effects should be minimal.

487 The experimental dyke geometry in profile is circular in the early stages of dyke growth. This
488 penny-shaped geometry is a consequence of intrusion into a homogeneous, isotropic elastic
489 solid; in nature however, anisotropy and mechanical heterogeneities of the crust are
490 expected to influence the shape of the dyke (e.g. Kavanagh and Sparks, 2011). Fluid may also
491 be fed into the dyke by a slit-like geometry rather than the nozzle-like injector we used. The
492 dyke geometry evolved to become elongate as it approached the surface, in response to an
493 accelerating dyke tip. In nature, mechanical heterogeneity of the crust will likely affect the
494 dyke ascent rate and whether or not such an acceleration would occur. In cross-section, our
495 experimental dyke developed a pinched tail and 'teardrop' morphology as the dyke
496 propagated through the tank towards eruption. This geometry is similar to that expected of
497 a 'Weertman crack', where a fixed volume injection ascends buoyantly though an elastic
498 material (Weertman, 1971). This geometry occurred despite the crack receiving a constant
499 flux of fluid, and remaining connected to the source (even if the connection is very small). Our
500 experimental results therefore suggest the Weertman-crack geometry is not restricted to
501 fixed volume injections, but can be developed by dykes that have sustained magma flux too.
502 The analytical models that describe the buoyant length of fluid-filled fractures propagating in
503 an elastic material therefore may not fully capture the dynamical processes of dyke ascent,
504 and so will need to be revisited in the context of these new experimental observations.

505 *4.3. Magma flow in nature*

506 Our understanding of the dynamics of magma flow in dykes is limited to observations of
507 volcanic fissure eruptions (e.g. Lundgren et al. 2013); where in the early stages of eruption
508 the magma exits along the fissure length, but rapidly the extrusion becomes focused at a few
509 vents due to flow channelisation. The crystalline magma within ancient, solidified dykes offers
510 the best access to the dyke; however, exposure is often limited to partial 2-dimensional
511 sections and unravelling syn- and post-emplacement textures from the time-sequence of
512 magma solidification is difficult. However, there are several macroscopic flow indicators that
513 can be used, including elongated vesicles that are aligned (e.g. Figure 7), scour marks (e.g.
514 Smith, 1987), phenocryst alignment (e.g. Bhattacharji and Smith, 1964), drag folds (e.g.
515 Walker et al. 2017) and cataclastic elongation of phenocrysts (Smith, 1987). Magnetic fabrics,
516 such as AMS have also been used to infer magma flow (e.g. Herrero Bervera et al. 2001).
517 Temporal variations in flow are postulated based on, for example, bubble-rich and bubble-
518 poor coupled bands that suggest pressure fluctuations (see Figure 7c and d). Any flow
519 indicator needs to be used with caution, especially as the final stages of magma flow may be
520 drainage or back-flow towards the source (e.g. Lundgren et al. 2013).

521 Our experimental results of the vectors of fluid flow during dyke intrusion and eruption
522 provides important dynamical constraints that will likely aid the interpretation of flow fabrics
523 within intrusions, in particular due to the identification of distinct stages of dyke ascent
524 leading to eruption. In our experiments, the fluid initially circulated in two jets as the pre-cut
525 was first filled and then the crack began to propagate. This particular flow pattern was
526 potentially an artefact of the initial injection conditions, and could have formed by the
527 injector being partially blocked by incomplete breaking of the petroleum jelly seal. This early

stage in the experimental dyke growth could vary between experiments and so directly comparing this early stage of the experiment with natural observations is not recommended. However, after this initial stage the dyke width and length increased at constant velocity and this was when we observed a single jet to form and circulation of fluid within the propagating dyke. This jet persisted from these early stages of dyke growth up to immediately prior to eruption, with rapid evacuation of the dyke when it breached the surface. Our experimental observations therefore suggest that fluid flow trajectories within a non-feeder dyke (that does not erupt) may be highly variable with upward, lateral and downward flow occurring. These would therefore be distinct from a feeder dyke where the flow velocity would be predominantly vertical, proffering the opportunity to assess whether or not a dyke erupted (even with limited exposure of the plumbing system) based on the flow vectors preserved but also depending on the timescale of solidification (e.g. Daniels et al. 2012). Jet formation and channelisation within natural dykes may occur in nature, resulting in progressive and preferred erosion of the country rock due to the sustained and rapid fluid flow, leading to the development of asymmetrical dyke geometries in the rock record (e.g. Kavanagh and Sparks, 2011). Variations in flow, either during intrusion or eruption, may lead to erosion of the mushy and progressively crystallising dyke margins. Our experimental dykes comprised a low viscosity Newtonian fluid, however during magma ascent it is likely that non-Newtonian fluid rheology such as shear-thinning will develop as the crystal and bubble-content of the magma increases. Future experiments will be required to assess the impact of non-Newtonian rheologies on the flow dynamics within a propagating dyke

4.4. Host-rock deformation in nature

The conceptual framework used in our laboratory study is that dykes can be modelled as hydraulic fractures that intrude an elastic material, which is in-keeping with assumptions used

552 during real-time monitoring and inversion modelling of intrusion-induced deformation at
553 active volcanoes. However, an important consideration in dyke ascent mechanics is
554 understanding under what circumstances they create their own fractures or instead intrude
555 pre-existing weak planes. This is important for hazard assessment and predicting the sites of
556 future vents from dyke ascent e.g. in a monogenetic volcanic field (e.g. Le Corvec et al. 2013b).
557 The sub-surface deformation patterns we observe in our experiments, such as incremental
558 strain and stress field evolution, could be helpful to interpret seismicity during active
559 intrusion. The surface deformation patterns could be helpful to inform the interpretation of
560 tilt meter data, GPS monitoring networks and InSAR analysis.

561 Field evidence of host deformation associated with dyke ascent ranges from macro- to micro-
562 scale. Dyke-parallel fractures at the dyke margins within sedimentary (Delaney et al. 1986)
563 or igneous host-rocks (Brown et al. 2007; Kavanagh and Sparks 2011) may suggest these were
564 pre-existing structures that were exploited by the ascending magma, although the
565 exploitation of existing fractures is likely to be a relatively near-surface process (Rubin, 1995).
566 A potentially valuable, yet unexplored tool to study the micro- scale damage zone
567 surrounding hydraulic fractures (e.g. dykes) are Fluid Inclusion Planes (FIPs). Fluid Inclusion
568 Planes (FIPs) appear under optical microscopy as small linear “bubble” trails in individual
569 crystals and are thought to be fossilised microfractures which are the result of healing, or
570 “necking down” of previously open fractures which functioned as fluid pathways (Roedder,
571 1984). FIPs can provide valuable information when studying rock deformation as they can
572 provide insight into deformation geometries, chronology of deformation (Lespinasse, 1999;
573 Pecher et al. 1985) and are potential indicators to the paleostress field (Lespinasse and
574 Pecher, 1986). The healing process is relatively quick in relation to geological time (Smith and
575 Evans, 1984) and they form as Mode I fractures, occur predominately perpendicular to the

576 least principal compressive stress axis, σ^3, with no evidence of shear displacement which
577 would be expected from Mode II/III fractures (Lespinasse 1999). Quartz is a common mineral
578 for FIPs to be observed as, due to its crystallographic properties, fractures in quartz are usually
579 formed in response to the regional stress field (Lespinasse and Cathelineau, 1990). Minerals
580 such as feldspars, however, which have more complex cryptographic features, such as
581 twinning and the presence of cleavages, can alter the preservation or have preferred
582 orientations of FIPs (Lespinasse 1999). Observations of FIPs can be made optically at
583 magnifications as low as x10, as shown in Figure 8a; however optical observations are
584 somewhat hindered due to the healing process, making many FIPs invisible in plane polarized
585 and cross polarised light. The use of a Scanning Electron Microscope fitted with a
586 Cathodoluminescent detector (SEM-CL) can dramatically increase the number of observable
587 FIPs by up to 100% in some cases. This is demonstrated in the optical micrograph Figure 8a,
588 which shows roughly 8 visible FIPs, compared to the SEM-CL micrograph Figure 8b, which has
589 16 potential FIPs. The SEM-CL provides a more complete image of FIPs, making it a more
590 effective structural tool to assess host-rock damage around dykes.

591 **5.0 Conclusions**

592 The laboratory methods we have employed have allowed the detailed description and
593 quantification of coupled fluid flow and host deformation during the inception, growth and
594 eruption of an experimental dyke. We have identified four phases of dyke ascent:

595 Stage 1: Dyke inception and early growth

596 • Fluid flow is complex, circulating as the dyke grows equally in breadth and
597 length creating a penny-shaped geometry. Sub-surface deformation is focused
598 at the growing tip, with material at the dyke tip margin progressively displaced

outwards and stress concentration showing a ‘bow-tie’ geometry. No surface elevation change is recorded as the dyke is formed and begins to grow.

Stage 2: Dyke propagation

- Fluid flow comprises a rapid, centralised, upward-rising pseudo-steady jet with slow down-welling at the dyke margin. Regions of static fluid develop within the circulating flow. Sub-surface deformation remains concentrated at the growing tip, shown by a concentration in incremental strain and stress. The dyke tail pinches almost-closed at depth at the end of this stage.

Stage 3: Near-surface ascent

- A flow instability develops as the upward and centralised rapid fluid flow begins to meander and move from side to side. Two jets at the base of the dyke feed into the upper single jet, and slower fluid continues to down-well at the growing dyke margin. The dyke begins to lengthen, developing an elliptical geometry as the dyke tip begins to accelerate towards the surface. The pinched tail of the ascending dyke migrates towards the surface. The dyke trajectory is deflected as shear stresses intensify, and the dyke stress field begins to interact with the surface. The inclined dyke produces an asymmetrical cumulative elevation change centred above the dyke.

Stage 4: Fissure eruption

- Rapid opening of the dyke occurs as it intersects the surface and produces a short fissure. This depressurisation causes rapid evacuation of fluid from the dyke. Flow is focused towards the vent and the active-region of flow is increasingly focused towards the surface as the pinched dyke tail zips closed from depth and accelerates towards the surface.

The experimental results emphasise the importance of considering coupled fluid flow and host deformation when developing the next generation of dyke ascent models, to inform the interpretation of the field and geophysical evidence of ancient, ongoing, and future dyke intrusion events.

Acknowledgements

JLK and DJCD acknowledge 'Living With Environmental Change' pump priming grants from the University of Liverpool, and a NERC Research Experience Placement from the Liverpool-Manchester EAO DTP that funded AJB. JLK acknowledges a Royal Society grant (RG130771). SHH acknowledges support from the Malaysian Government and the National University of Malaysia. EW thanks a NERC DTP PhD studentship. SM acknowledges support from a Mineralogical Society Postgraduate Student Bursary which funded fieldwork to Skye. All authors thank the University of Liverpool, Silvio De Angelis and Rob Duller for their assistance with the Micro Epsilon laser scanner, and Sarah Henton De Angelis for assistance with the SEM. Joan Martí, Lionel Wilson and Tim Horscroft are thanked for the invitation to write this research paper. Carmen López and Agust Gudmundsson are thanked for thoughtful reviews that improved the manuscript, and Joan Martí is thanked for editorial support.

639 **References**

640 Abdelmalak, M.M. et al., 2012. Fracture mode analysis and related surface deformation
641 during dyke intrusion Results from 2D experimental modelling. Earth and Planetary Science
642 Letters, 359-360(C), pp.93–105.

643 Adrian, R.J., 1991. Particle-imaging techniques for experimental fluid mechanics. Annual
644 Review of Fluid Mechanics, 23, pp.261–304.

645 Bhattacharji, S. & Smith, C.H., 1964. Flowage differentiation. Science, 145, pp.150–153.

646 Brizzi, S. et al., 2016. Salt matters: How salt affects the rheological and physical properties of
647 gelatine for analogue modelling. 679, pp.88–101.

648 Brown, R.J. et al., 2007. Mechanically disrupted and chemically weakened zones in segmented
649 dike systems cause vent localization: Evidence from kimberlite volcanic systems. Geology,
650 35(9), pp.815–818.

651 Caricchi, L., et al., 2014a. Frequency and magnitude of volcanic eruptions controlled by
652 magma injection and buoyancy. Nature Geoscience, 7(2), pp.1–5.

653 Caricchi, L., et al., 2014b. The influence of cooling, crystallisation and re-melting on the
654 interpretation of geodetic signals in volcanic systems. Earth and Planetary Science Letters,
655 388(C), pp.166–174.

656 Castro, J.M. et al., 2016. Rapid laccolith intrusion driven by explosive volcanic eruption.
657 Nature Communications, 7, pp.1–7.

658 Cervelli, P. et al., 2002. The 12 September 1999 Upper East Rift Zone dike intrusion at Kilauea
659 Volcano, Hawaii. Journal of Geophysical Research, 107(B7), 2150.

660 Crisp, J.A., 1984. Rates of magma emplacement and volcanic output. Journal of Volcanology
661 and Geothermal Research, 20, pp.177–211.

662 Dahm, T., 2000. On the shape and velocity of fluid-filled fractures in the Earth. Geophysical
663 Journal International, 142(1), pp.181–192.

664 Daniels, K.A. & Menand, T., 2015. An experimental investigation of dyke injection under
665 regional extensional stress. *Journal of Geophysical Research-Solid Earth*, 120, pp.2014–
666 2035.

667 Daniels, K.A. et al., 2012. The shapes of dikes: evidence for the influence of cooling and
668 inelastic deformation. GSA Bulletin, 124(7-8), pp.1102–1112.

669 Delaney, P.T. et al., 1986. Field relations between dikes and joints: Emplacement processes
670 and palaeostress analysis. Journal of Geophysical Research, 91(B5), pp.4920–4938.

671 Djabourov, M., Leblond, J. & Papon, P., 1988. Gelation of aqueous gelatin solutions. II.
672 Rheology of the sol-gel transition. Journal de Physique, 49(2), pp.333–343.

673 Geshi, N., Kusumoto, S. & Gudmundsson, A., 2010. Geometric difference between non-feeder
674 and feeder dikes. Geology, 38(3), pp.195–198.

675 Gudmundsson, A., 2002. Emplacement and arrest of sheets and dykes in central volcanoes.
676 Journal of Volcanology and Geothermal Research, 116, pp.279–298.

677 Gudmundsson, A., 2003. Surface stresses associated with arrested dykes in rift zones. Bulletin
678 of volcanology, 65(8), pp.606–619.

679 Gudmundsson, A., 2006. How local stresses control magma-chamber ruptures, dyke
680 injections, and eruptions in composite volcanoes. Earth-Science Reviews, 79(1-2), pp.1–31.

681 Gudmundsson, A. et al., 2014. Dike emplacement at Bardarbunga, Iceland, induces unusual
682 stress changes, caldera deformation, and earthquakes. Bulletin of volcanology, 76(10),
683 p.869.

684 González, P.J. & Palano, M., 2014. Mt. Etna 2001 eruption: New insights into the magmatic
685 feeding system and the mechanical response of the western flank from a detailed geodetic
686 dataset. Journal of Volcanology and Geothermal Research, 274, pp.108–121.

687 Herrero-Bervera, E. et al., 2001. Magnetic fabric and inferred flow direction of dikes,
688 conesheets and sill swarms, Isle of Skye, Scotland. Journal of Volcanology and Geothermal
689 Research, 106(3), pp.195–210.

690 Ilyinskaya, E. et al., 2017. Earth and Planetary Science Letters. Earth and Planetary Science
691 Letters, pp.1–14.

692 Kahl, M. et al., 2011. Dynamic plumbing system beneath volcanoes revealed by kinetic
693 modeling, and the connection to monitoring data: An example from Mt. Etna. Earth and
694 Planetary Science Letters, 308, pp.11–12.

695 Kavanagh, J., Menand, T. & Daniels, K.A., 2013. Gelatine as a crustal analogue: Determining
696 elastic properties for modelling magmatic intrusions. Tectonophysics, 582, pp.101–111.

697 Kavanagh, J.L. & Sparks, R.S.J., 2011. Insights of dyke emplacement mechanics from detailed
698 3D dyke thickness datasets. Journal of the Geological Society, 168(4), pp.965–978.

699 Kavanagh, J.L. et al., 2017. Controls on sill and dyke-sill hybrid geometry and propagation in
700 the crust: The role of fracture toughness. Tectonophysics, 698(C), pp.109–120.

701 Kavanagh, J.L., Boutelier, D. & Cruden, A.R., 2015. The mechanics of sill inception, propagation
702 and growth: Experimental evidence for rapid reduction in magmatic overpressure. Earth
703 and Planetary Science Letters, 421, pp.117–128.

704 Kavanagh, J. L., 2018. Mechanisms of magma transport in the upper crust – Dyking. In:
705 Burchardt, S. (ed.), Volcanic and Igneous Plumbing Systems: Understanding Magma
706 Transport, Storage, and Evolution in the Earth's Crust. Elsevier. In press.

707 Kavanagh, J. L., Engwell, S., and Martin, S., In Review. A review of laboratory and numerical
708 modelling in volcanology, Solid Earth Discussions., https://doi.org/10.5194/se-2017-40.

709 Kavanagh, J.L., Menand, T. & Sparks, R.S.J., 2006. An experimental investigation of sill
710 formation and propagation in layered elastic media. Earth and Planetary Science Letters,
711 245(3-4), pp.799–813.

712 Le Corvec, N., Menand, T. & Lindsay, J., 2013a. Interaction of ascending magma with pre-
713 existing crustal fractures in monogenetic basaltic volcanism: an experimental approach.
714 Journal of Geophysical Research-Solid Earth, 118(3), pp.968–984.

715 Le Corvec, N., Spörli, K.B., et al., 2013b. Spatial distribution and alignments of volcanic
716 centers: Clues to the formation of monogenetic volcanic fields. Earth-Science Reviews,
717 124(C), pp.1–19.

718 Lespinasse, M., 1999. Are fluid inclusion planes useful in structural geology? Journal of
719 Structural Geology, 21, pp.1237–1243.

720 Lespinasse, M. & Cathelineau, M., 1990. Fluid percolations in a fault zone: a study of fluid
721 inclusion planes in the St Sylvestre granite, northwest Massif Central, France.
722 Tectonophysics, 184, pp.173–187.

723 Lespinasse, M. & Pecher, A., 1986. Microfracturing and regional stress field: a study of the
724 preferred orientations of fluid-inclusion planes in a granite from the Massif Central, France.
725 Journal of Structural Geology, 8(2), pp.169–180.

726 Lister, J.R., 1990a. Buoyancy-driven fluid fracture: similarity solutions for the horizontal and
727 vertical propagation of fluid-filled cracks. Journal of Fluid Mechanics, 217, pp.213–239.

728 Lister, J.R., 1990b. Buoyancy-driven fluid fracture: the effects of material toughness and of
729 low-viscosity precursors. Journal of Fluid Mechanics, 210, pp.263–280.

730 Lister, J.R. & Kerr, R.C., 1991. Fluid-mechanical models of crack propagation and their
731 application to magma transport in dykes. Journal of Geophysical Research-Solid Earth,
732 96(B6), pp.10049–10077.

733 Lundgren, P. et al., 2013. Evolution of dike opening during the March 2011 Kamoamoa fissure
734 eruption, Kīlauea Volcano, Hawai`i. Journal of Geophysical Research-Solid Earth, 118(3),
735 pp.897–914.

736 Maccaferri, F. et al., 2014. Off-rift volcanism in rift zones determined by crustal unloading.
737 Nature Geoscience, 7(4), pp.297–300.

738 Menand, T., Daniels, K.A. & Benghiat, P., 2010. Dyke propagation and sill formation in a
739 compressive tectonic environment. Journal of Geophysical Research, 115(B08201),
740 doi:10.1029–2009JB006791.

741 Menand, T., de Saint-Blanquat, M. & Annen, C., 2011. Emplacement of magma pulses and
742 growth of magma bodies. Tectonophysics, 500(1-4), pp.11–19.

743 Patane, D. et al., 2002. Tomographic images and 3D earthquake locations of the seismic
744 swarm preceding the 2001 Mt. Etna eruption: Evidence for a dyke intrusion. Geophysical
745 Research Letters, 29(10), 1497.

746 Pecher, A., Lespinasse, M. & Leroy, J., 1985. Relations between fluid inclusion trails and
747 regional stress field: A tool for fluid chronology—An example of an intragranitic uranium
748 ore deposit (northwest Massif Central, France). Lithos, 18, pp.229–237.

749 Pinel, V. & Jaupart, C., 2000. The effect of edifice load on magma ascent beneath a volcano.
750 Philosophical Transactions of the Royal Society A: Mathematical, Physical and Engineering
751 Sciences, 358(1770), pp.1515–1532.

752 Putirka, K.D., 2017. Down the Crater: Where Magmas are Stored and Why They Erupt.
753 Elements, 13, pp.11–16.

754 Righetti, R. et al., 2004. The feasibility of using elastography for imaging the Poisson's ratio in
755 porous media. Ultrasound in medicine & biology, 30(2), pp.215–228.

756 Rivalta, E. et al., 2015. A review of mechanical models of dike propagation: Schools of thought,
757 results and future directions. Tectonophysics, 638, pp.1–42.

758 Rivalta, E., Böttinger, M. & Dahm, T., 2005. Buoyancy-driven fracture ascent: Experiments in
759 layered gelatine. Journal of Volcanology and Geothermal Research, 144(1-4), pp.273–285.

760 Roedder, E., 1984. Fluid Inclusions. Reviews in Mineralogy, 12, pp. 646.

761 Roper, S.M. & Lister, J.R., 2007. Buoyancy-driven crack propagation: the limit of large fracture
762 toughness. Journal of Fluid Mechanics, 580, pp.359–380.

763 Rubin, A.M., 1995. Propagation of Magma-Filled Cracks. Annual Reviews in Earth and
764 Planetary Sciences, 23(1), pp.287–336.

765 Sigmundsson, F. et al., 2010. Intrusion triggering of the 2010 Eyjafjallajökull explosive
766 eruption. Nature, 468(7322), pp.426–430.

767 Sigmundsson, F. et al., 2014. Segmented lateral dyke growth in a rifting event at Ba´rðarbunga
768 volcanic system, Iceland. Nature, 517(7533), pp.191–195.

769 Smith, R. P., 1987. Dyke emplacement at Spanish Peaks, Colorado. In: Halls, H.C., Mafic dyke
770 swarms, Geological Association of Canada Special Paper, 34, pp.47-54.

771 Smith, D.L., Evans, B., 1984. Diffusional crack healing in quartz. Journal of Geophysical
772 Research, 89, p.4125-4135.

773 Sparks, R., Biggs, J. & Neuberg, J.W., 2012. Monitoring volcanoes. Science, 335, pp.1310–
774 1311.

775 Spence, D.A., Sharp, P.W. & Turcotte, D.L., 1987. Buoyancy-driven crack propagation: a
776 mechanism for magma migration. Journal of Fluid Mechanics, 174, pp.135–153.

777 Taisne, B. & Jaupart, C., 2009. Dike propagation through layered rocks. Journal of Geophysical
778 Research-Solid Earth, 114(B9), doi:10.1029–2008JB006228.

779 Taisne, B. & Tait, S., 2011. Effect of solidification on a propagating dike. Journal of Geophysical
780 Research, 116(B1), B01206.

781 Taisne, B. & Tait, S., 2009. Eruption versus intrusion? Arrest of propagation of constant
782 volume, buoyant, liquid-filled cracks in an elastic, brittle host. Journal of Geophysical
783 Research, 114(B6), B06202.

784 Takada, A., 1990. Experimental study on propagation of liquid-filled crack in gelatin: shape
785 and velocity in hydrostatic stress condition. Journal of Geophysical Research, 95, pp.8471–
786 8481.

787 Walker, R.J., Branney, M.J. & Norry, M.J., 2017. Dike propagation and magma flow in a glassy
788 rhyolite dike: A structural and kinematic analysis. Geological Society of America Bulletin,
789 B31378.1.

790 Watanabe, T. et al., 2002. Analogue experiments on magma-filled cracks: competition
791 between external stresses and internal pressure. Earth Planets and Space, 54, pp.1247–
792 1261.

793 Weertman, J., 1971. Theory of water-filled crevasses in glaciers applied to vertical magma
794 transport beneath oceanic ridges. Journal of Geophysical Research, 76(5), pp.1171–1183.

795 Wright, T.J. et al., 2012. Geophysical constraints on the dynamics of spreading centres from
796 rifting episodes on land. Nature Geoscience, 5, pp.242–250.

Experiment # (Ref)	X (wt%)	H (m)	ρ (kg/m^3)	T_{mix} (ºC)	T (ºC)	t_{set} (hr)	Q (m^3/s)	E (Pa)	t (s)	Technique
1 (SD07)	2.5	0.24	1002.5	24	5	24	3.9 x10^{-7}	2921	480	Pol, Surf Def
2 (SD09)	2.5	0.24	1002.5	23	5	23	3.9 x10^{-7}	3042	500	Pol, Surf Def
3 (AJB01)	2.5	0.25	1002.5	22	5	16	3.9 x10^{-7}	2030	416	PIV
4 (AJB02)	2.5	0.25	1002.5	21	5	15.5	3.9 x10^{-7}	2030	405	DIC

Table 1. Experiment parameters and variables. X = gelatine concentration, H = gelatine layer depth, ρ = gelatine density, T_{mix} = temperature of gelatine mixture when left to solidify, T = gelatine temperature when experiment commenced, t_{set} = time cooling, Q = injection flux, E = Young's modulus, t = time to eruption, and Technique = experimental imaging and analysis technique applied (Pol = polarized light, Surf Def = surface elevation change monitoring, PIV = particle image velocimetry, DIC = digital image correlation).

802

	Geometry	Material	m (kg)	a (m)
Load A	Cylinder	Brass	0.0501	0.0125
Load B	Cylinder	Brass	0.0418	0.0125

803

804 **Table 2:** Properties of experimental loads used to calculate Young's modulus of the solidified
805 gelatine prior to running an experiment, where 'm' is the mass of the load and 'a' is its radius.

Figures and captions

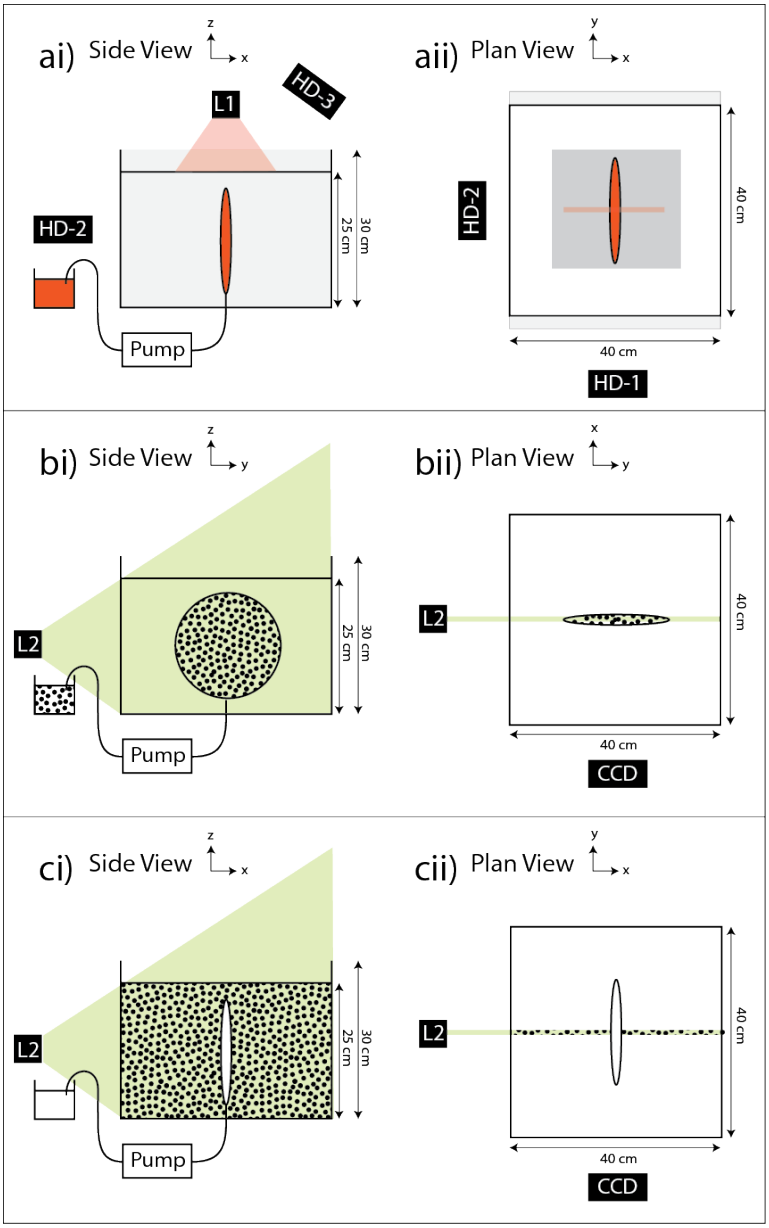

Figure 1: Schematic sketch of three apparatus setups for imaging dyke experiments where water is injected into the base of a gelatine slab using a peristaltic pump. a) Two polarising sheets (pale grey) are attached to the outside of the tank in the x-z plane. An overhead laser (L1) monitors surface elevation change along a line projected onto the sand-covered gelatine surface (x-y plane), centred on the injection point and perpendicular to the dyke strike-direction. Three HD cameras monitor the growth of the dyke (HD-1 x-z plane, HD-2 y-z plane, and HD-3 x-y plane). b) Particle image velocimetry: a CCD camera (y-z plane) records fluorescing passive-tracer particles within the injected fluid, in a vertical laser sheet projected through the gelatine (centred on the injector, and parallel to the dyke strike-direction). c) Digital image correlation: a CCD camera (x-z plane) records a vertical laser-illuminated sheet through the gelatine, which contains suspended passive-tracer particles (centred on the injector, perpendicular to the dyke strike-direction). Side (i) and plan (ii) views are shown for each method.

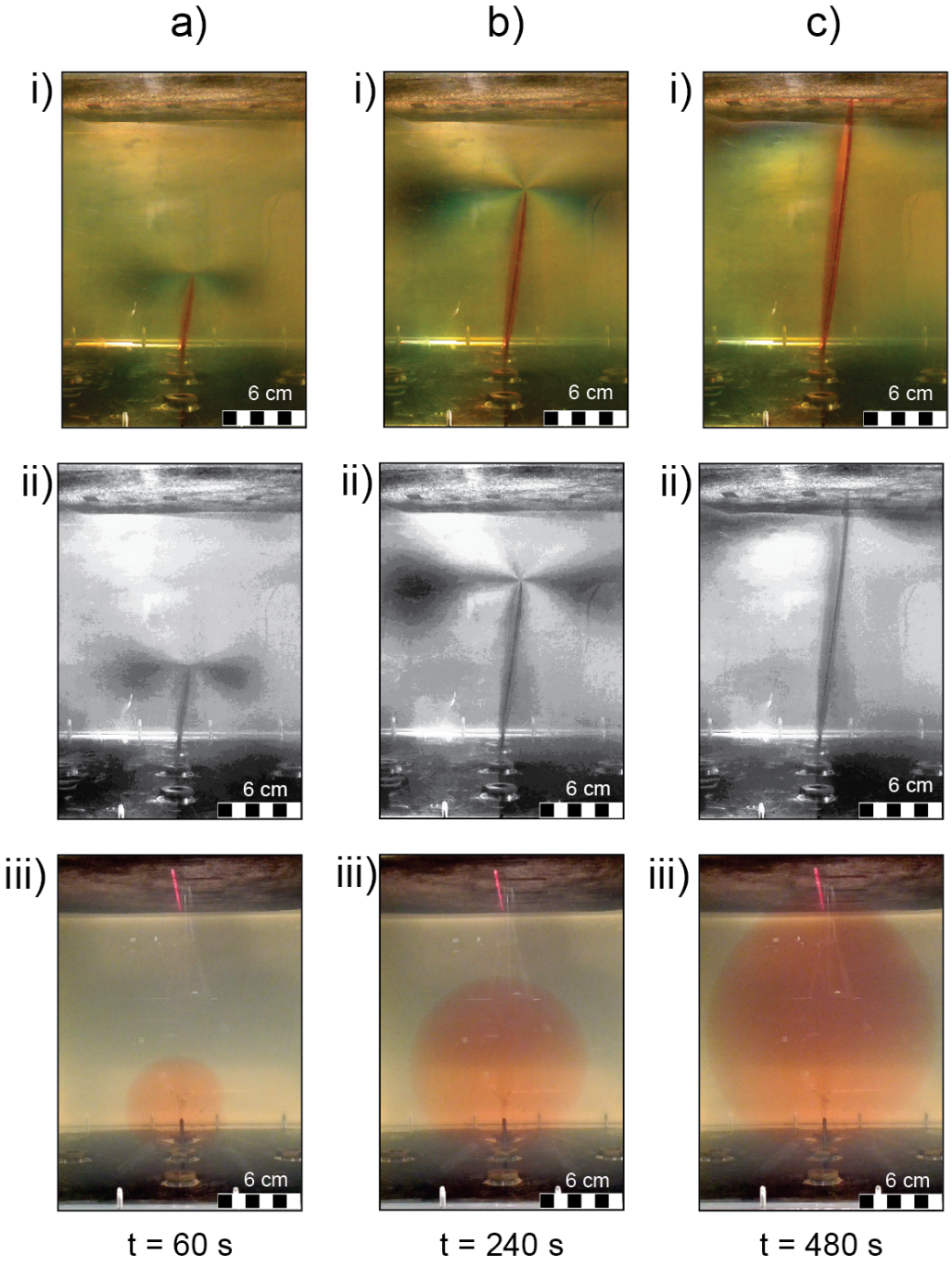

Figure 2: Series of cropped photographs showing the evolution of stress in the gelatine during dyke ascent at 3 time steps: a) 60 seconds, 240 seconds and 480 seconds. The position of the overhead laser is clear in all colour images as a red line at the top of the frame. (i) Polarised light, where the photoelasticity of gelatine produces colour fringes that relate to stress intensity, and (ii) these images converted to greyscale to show the stress pattern more clearly. (iii) A perpendicular view of the dyke growth showing the typical penny-shape. (Experiment 1; see Table 1, Figure 1a and Supplementary Video S1).

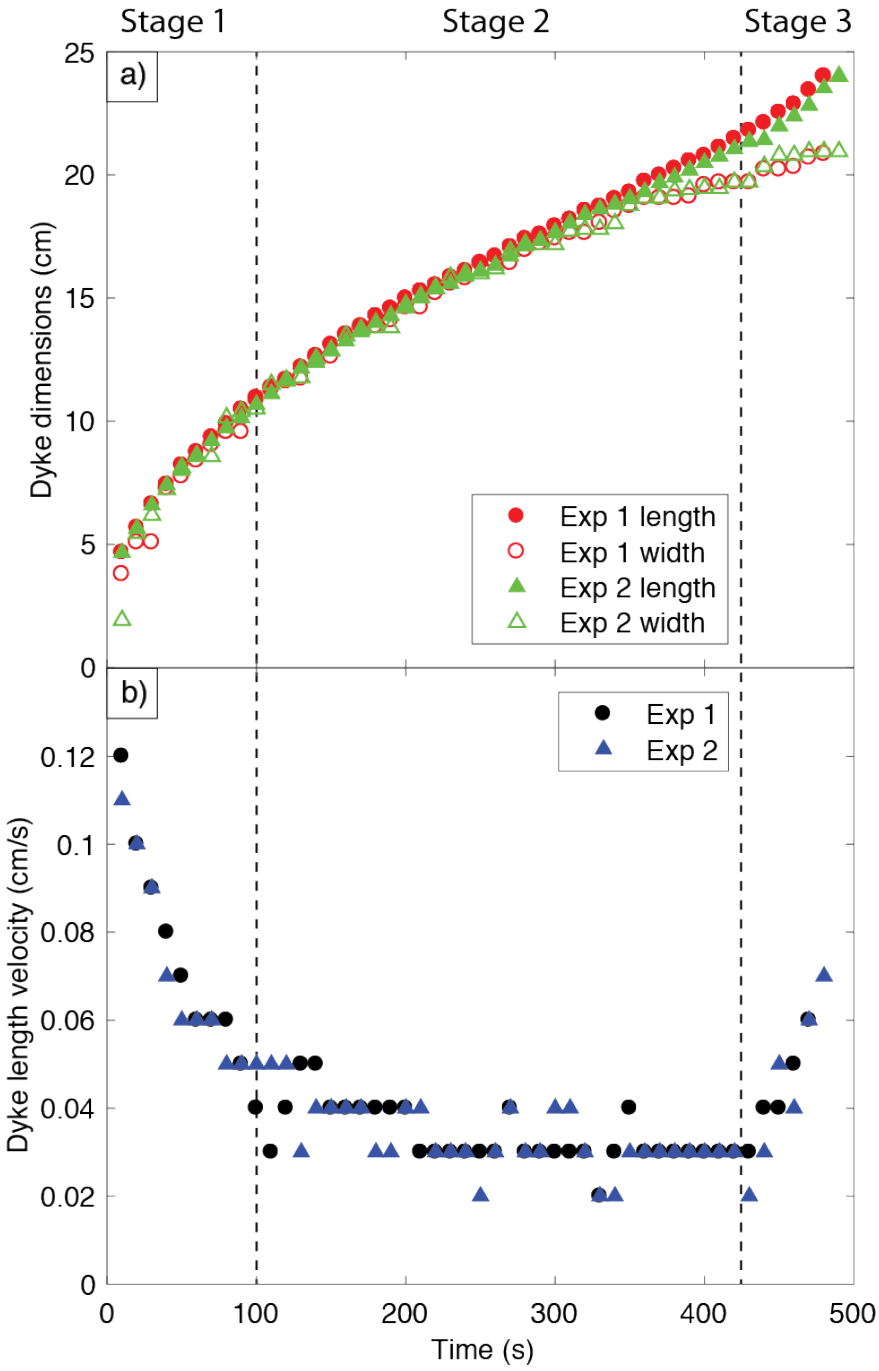

832
833 **Figure 3:** Three of four stages of dyke growth in length and width over time: a) Dyke length
834 and width, and b) dyke length velocity. Data from two equivalent experiments are shown (see
835 Table 1) up to the point of eruption, measured from the base of the injector. Stage 4 is not
836 shown, but occurs at the end of the experiment as the dyke erupts.

837

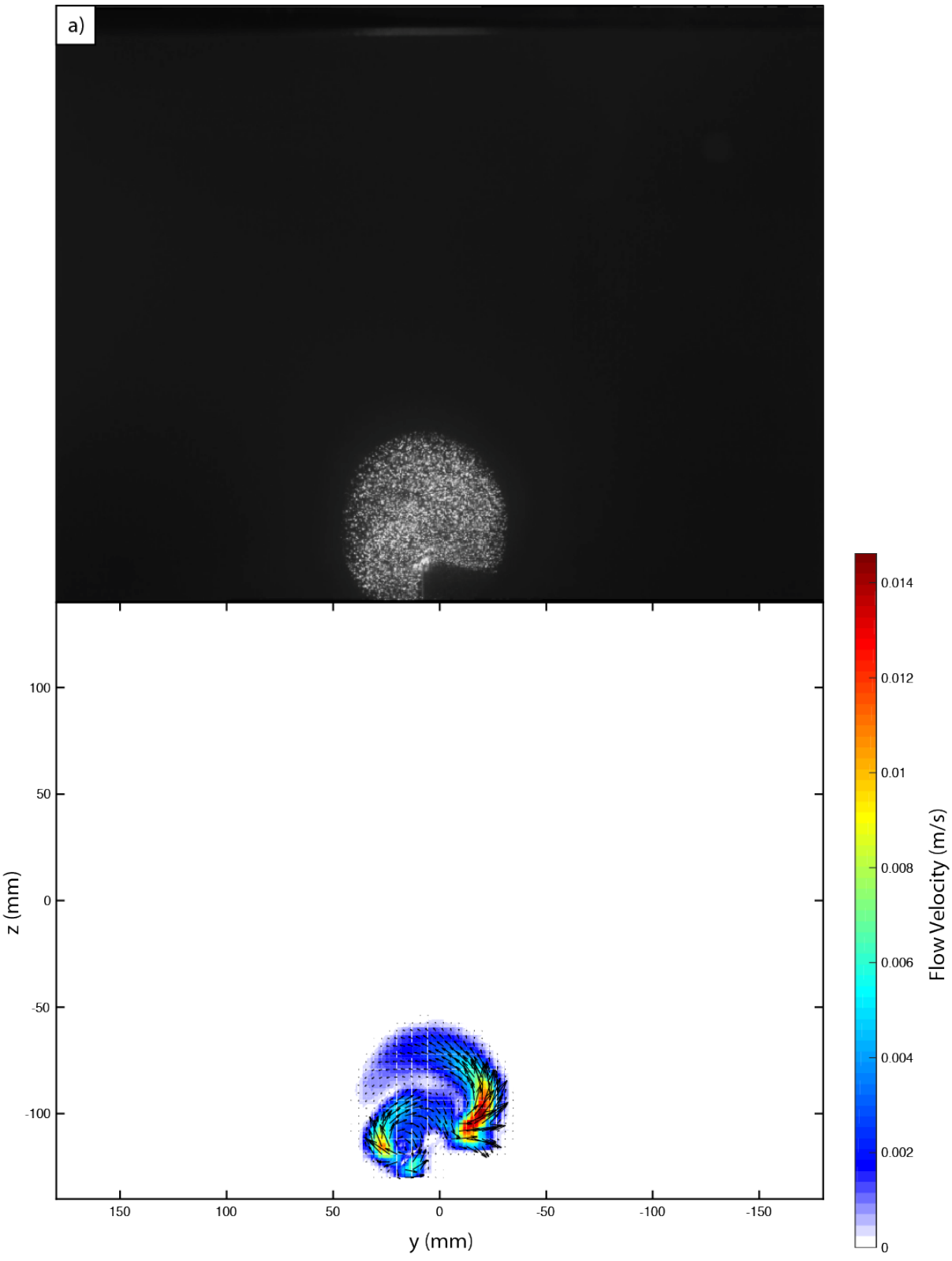
a)
100
50
0
-50
-100
z (mm)
150
100
50
0
-50
-100
-150
y (mm)
0.014
0.012
0.01
0.008
0.006
0.004
0.002
0
Flow Velocity (m/s)

838

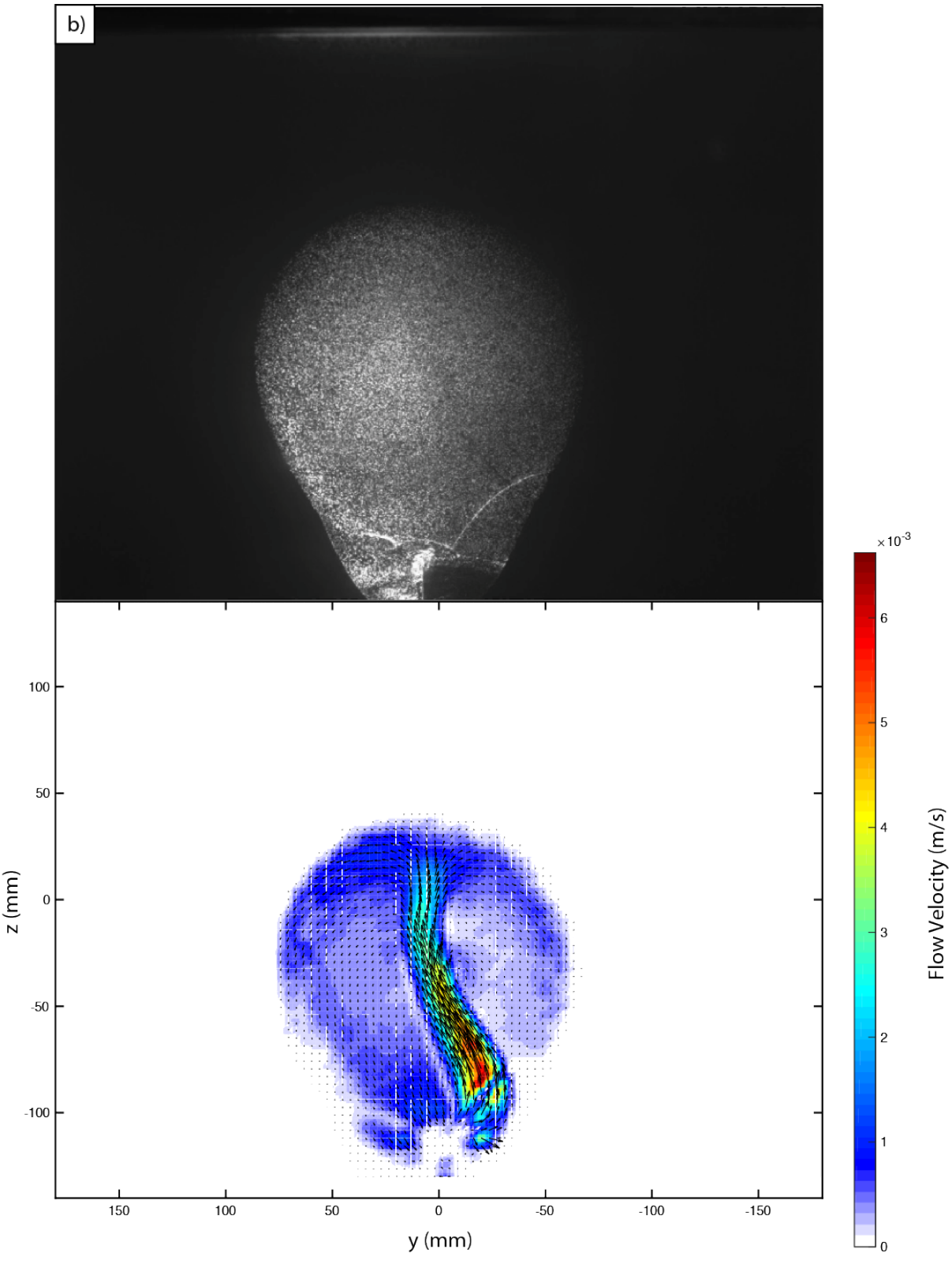
b)
100
50
0
-50
-100
z (mm)
150
100
50
0
-50
-100
-150
y (mm)
×10^-3
6
5
4
3
2
1
0
Flow Velocity (m/s)

839

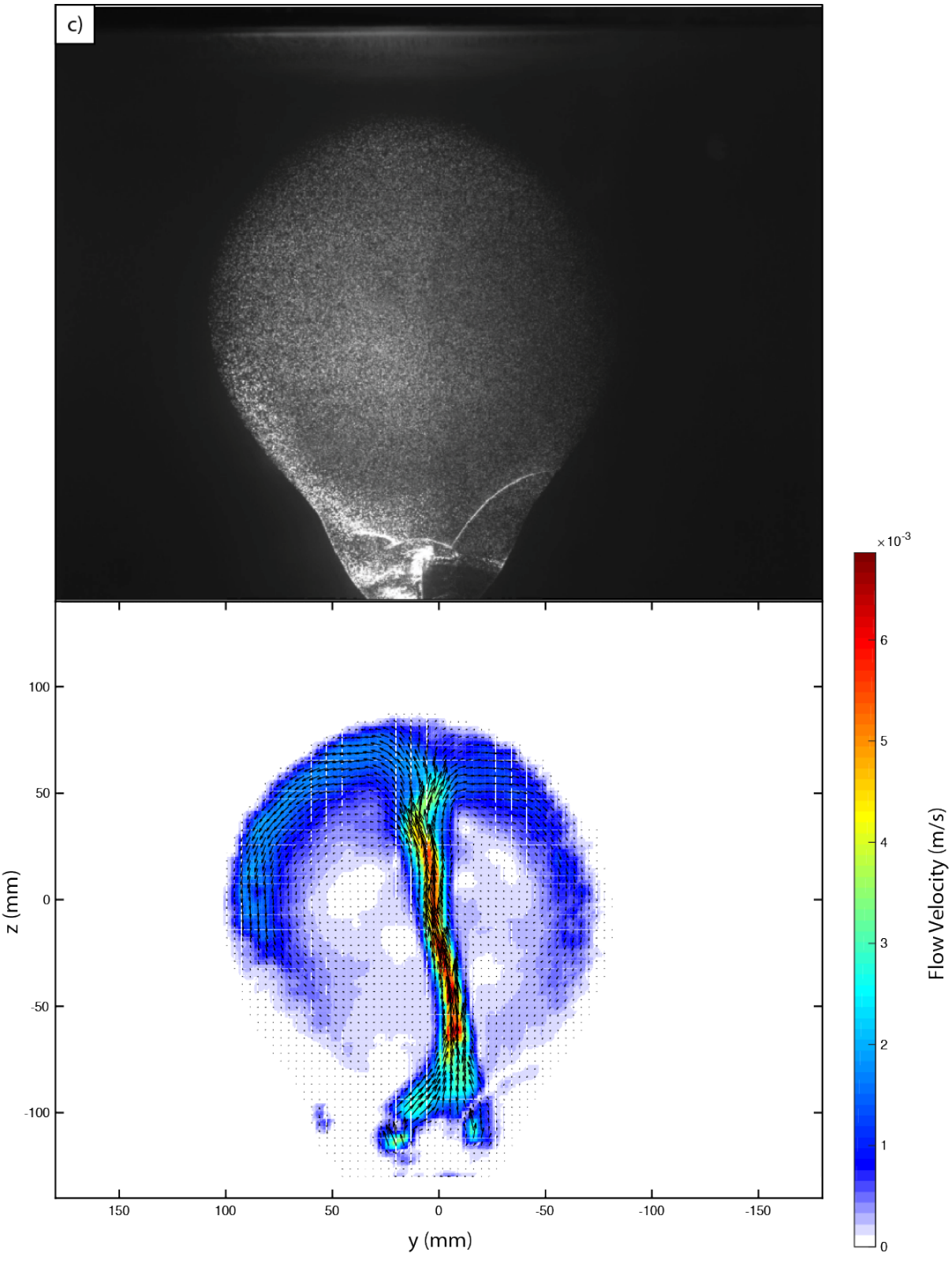
c)
100
50
0
-50
-100
z (mm)
150
100
50
0
-50
-100
-150
y (mm)
×10^-3
6
5
4
3
2
1
0
Flow Velocity (m/s)

840

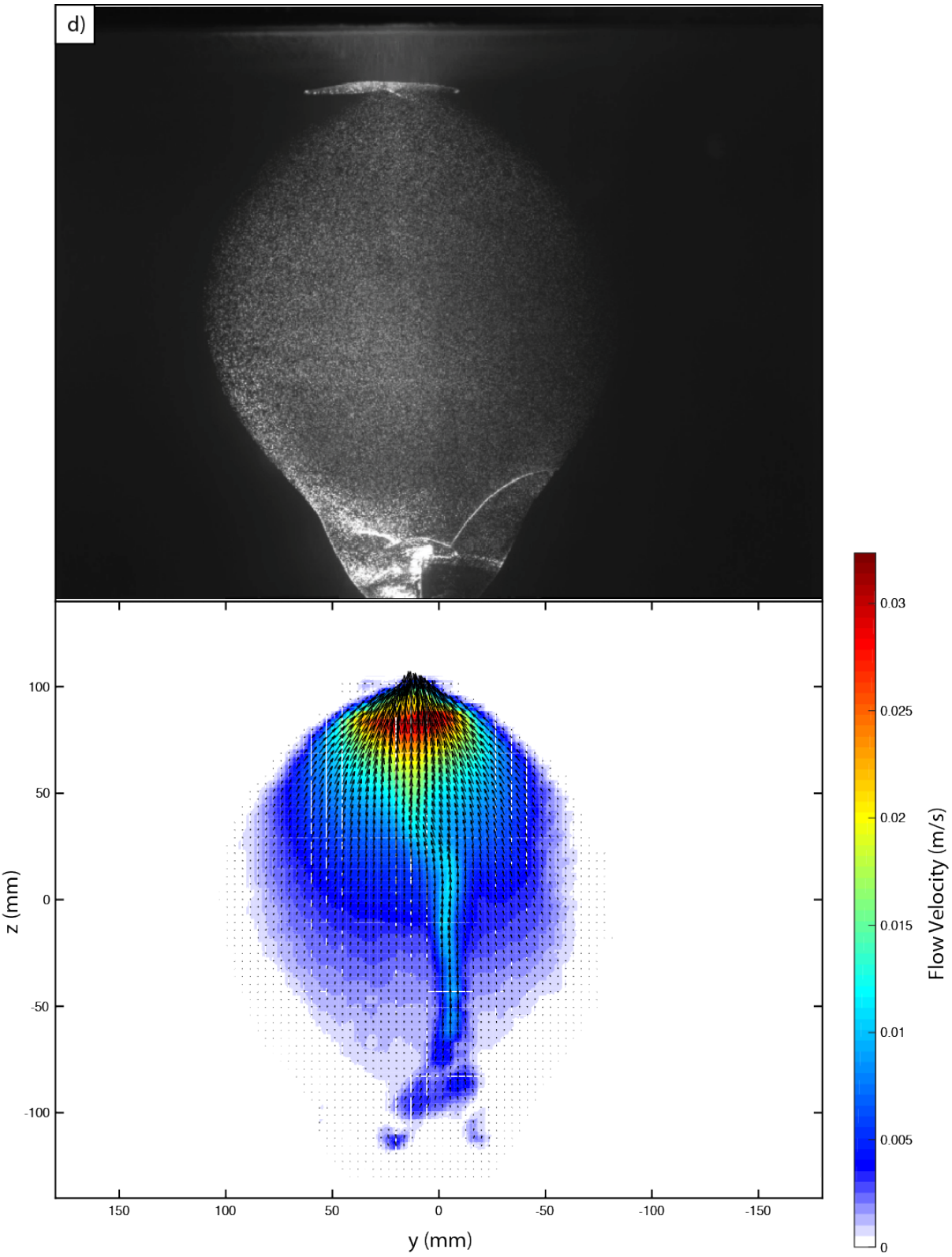

Figure 4: Four stages of fluid flow within a propagating experimental dyke (Experiment 3), quantified using PIV. Flow velocities (m/s) are shown as vectors (black arrows) and magnitude (colour map). See Supplementary Video S2. a) Stage 1: initial growth (frame 500, 56 s), b) Stage 2: established dyke (frame 2000, 225 s), c) Stage 3, instability development in jet (frame 3500, 396 s), and d) Stage 4: fissure eruption (frame 3691, 416 s).

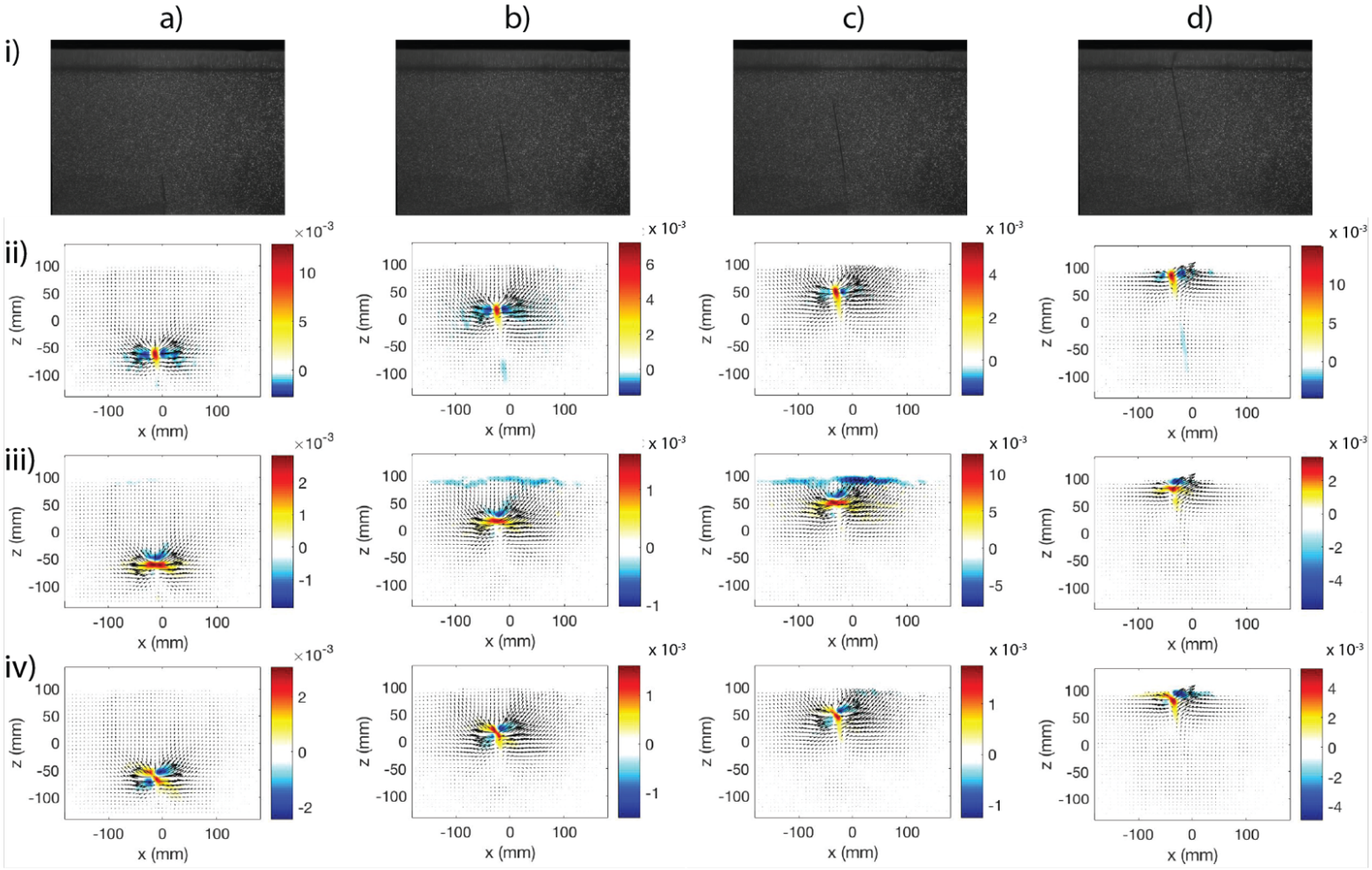

Figure 5: Four stages of sub-surface incremental strain evolution (colour maps) of experimental dyke ascent to eruption (Experiment 4): i) the de-warped experimental images, ii) ϵ_{xx}, (iii) ϵ_{zz} and (iv) ϵ_{xz}. Displacement is indicated (black arrows), and the DIC analysis is averaged over 10 frames. See Supplementary Video S3. a) Stage 1, dyke inception (frames 55-64, 55 s), b) Stage 2, dyke growth and ascent (frames 205-214, 205 s), c) Stage 3, immediately prior to eruption (frames 400-409, 400 s), and d) Stage 4, fissure eruption (frames 405-414, 405 s).

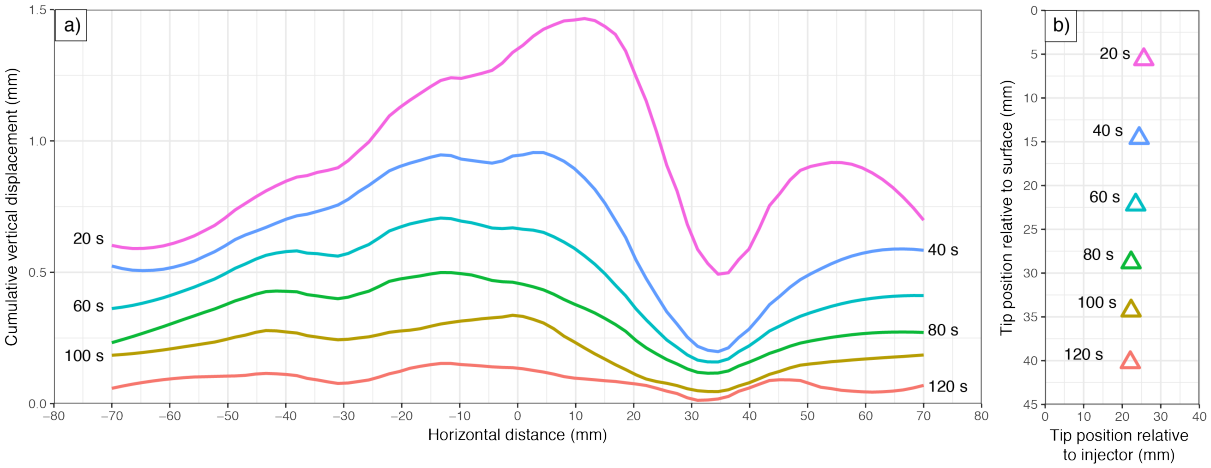

Figure 6: A series of surface deformation profiles according to dyke tip position of Experiment 1: a) Cumulative surface deformation from 120-20 seconds prior to eruption, where asymmetric topographic highs are produced either side of the dyke tip as it approaches eruption. b) Depth and lateral position of the dyke tip at 20 second intervals before eruption, noting that the tip has gradually deviated from vertical (0 mm) by up to 25.6 mm at 20 s prior to eruption.

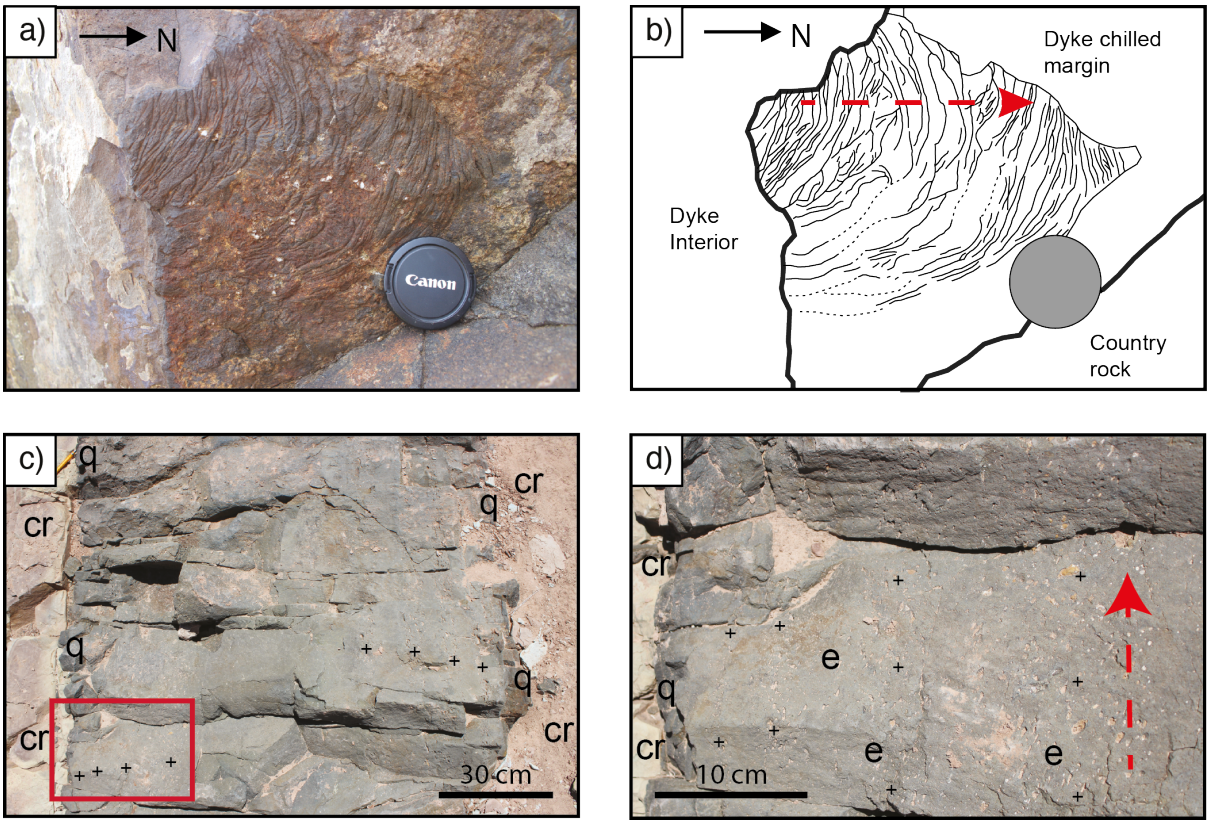

Figure 7: Field-scale features where orientations of magma flow are preserved within solidified dykes in different planes. a) Dyke's y-z plane: Photograph of a quarry face showing a basaltic dyke margin (Isle of Skye, Scotland); the country rock has eroded away to reveal ropey structures preserved at the contact. b) Complementary sketch diagram of a): ropey structures (thin-solid and thin-dashed lines) on the dyke chilled margin, and the inferred local palaeo-flow direction (red dashed arrow). c) Dyke's x-y plane: Photograph of a complete cross-section of a basaltic dyke viewed from above (San Rafael subvolcanic field, Utah); quenched (q) chilled margins against the country rock (cr), and cm-thick vesicle-rich bands (+) that are bound by vesicle-poor bands and parallel to the dyke margins. The position of the zoomed image (d) is indicated (red box). d) Zoomed photograph of c) additionally showing the location of elongated vesicles (e) within the dyke interior.

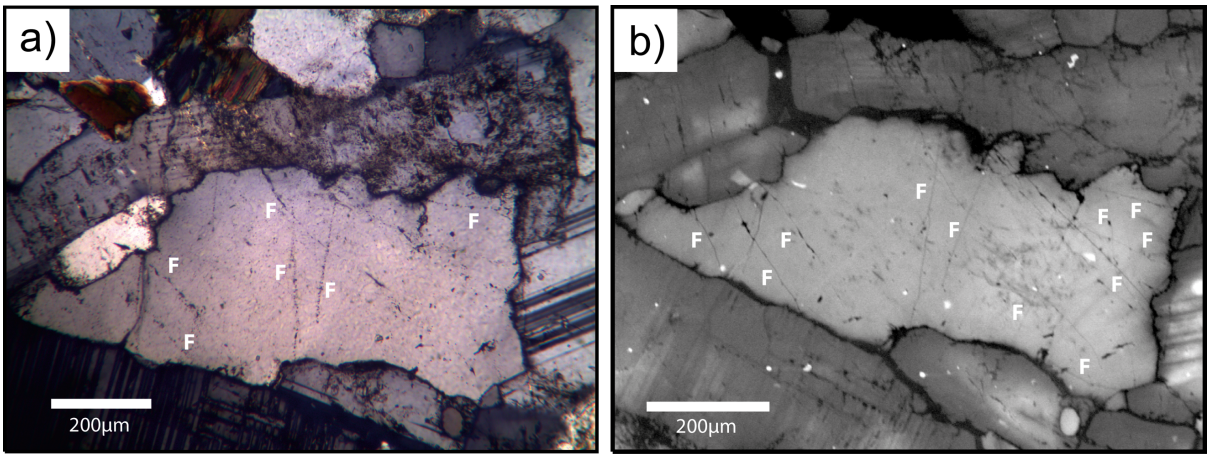

Figure 8: a) Optical photomicrograph in cross polarised light showing fluid inclusion planes (F) within quartz. b) SEM-Cathodoluminescent image showing comparative view of microfractures visible, note the increased detail and abundancy of FIPs (F).

Supplementary Figures Captions

Supplementary Video Figure S1: Video of sub-surface and surface dyke ascent imaged using polarised light (Experiment 1): a) camera HD-1, b) camera HD-2, and c) camera HD-3.

Supplementary Video Figure S2: Experiment to visualise and measure flow within a propagating dyke (Experiment 3) using PIV: a) Time-lapse video created from CCD camera images, and b) video of fluid flow velocities within the growing dyke (note the colour bar of velocity and the vector arrow scales change between frames).

Supplementary Video Figure S3: Experiment to visualise and measure sub-surface incremental strain evolution in the host material around a growing dyke (Experiment 4): a) Time-lapse video created from CCD camera images, and b) video of incremental strain (colour map) and displacement (arrows). Note the colour bar and the vector arrow scales change between frames.